SCANNING NEAR-FIELD OPTICAL MICROSCOPY FOR MEASURING MATERIALS PROPERTIES AT THE NANOSCALE

by

Larissa V. Stebounova

BS, Moscow Institute of Physics and Technology, 1999

MS, University of Pittsburgh, 2003

Submitted to the Graduate Faculty of

University of Pittsburgh in partial fulfillment

of the requirements for the degree of

Doctor of Philosophy

University of Pittsburgh

2005

UNIVERSITY OF PITTSBURGH

FACULTY OF ARTS AND SCIENCES

This dissertation was presented

by

Larissa V. Stebounova

It was defended on

April 18, 2005

and approved by

Prof. Shigeru Amemiya

Prof. David H. Waldeck

Prof. Jeremy Levy

Prof. Gilbert C. Walker

Dissertation Director

SCANNING NEAR-FIELD OPTICAL MICROSCOPY FOR MEASURING MATERIALS PROPERTIES AT THE NANOSCALE

Larissa V. Stebounova, PhD

University of Pittsburgh, 2005

ABSTRACT

Apertureless scanning near-field optical microscopy is a valuable tool for characterization of chemical and spectroscopic properties of the materials at the nanoscale. Description of apertureless near-field microscope is provided along with the description of a homodyne detection of the near-field signal which allows enhancing of a weak scattered radiation. Experimental evidences that homodyne detection markedly improves the signal-to-noise ratio of the detected signal are presented. A model for the dependence of the near field signal, as a function of the normal distance of the tip from the surface, is discussed. Application of a model in which the tip is represented by two spherical scatterers, one large and one small, indicates the electromagnetic field enhancement is 90 fold greater at the sharp apex of metallic probe tip.

Apertureless near-field scanning infrared microscopy was employed to study samples patterned with regions of DNA and hexadecanethiol. Chemical contrast imaging was achieved by examining IR absorption in the spectral region of the phosphate stretching band of DNA molecules and harmonic demodulation of the signal scattered by the oscillating probe. IR absorption maps revealed that the IR signal was not coupled to the vertical tip motion, indicating artifact-free imaging. Monolayer-sensitive chemical imaging with a lateral spatial resolution of approximately 200 nm is demonstrated.

The field enhancement in very small aperture lasers was studied using apertureless near-field microscopy. The near-field optical pattern around the aperture indicates the interference of surface plasmons with incident light. A surface plasmon point-source model has been used to determine the wavelength and the decay length of surface plasmons at the Al/silicon nitride interface. Near-field measurements also confirmed a preferred orientation of the rectangular aperture waveguide for the signal enhancement in very small aperture lasers.

Optical field confinement in a ridge waveguide nanostructure designed for ultrahigh-density recording was observed using an apertureless near-field scanning optical microscope. The aperture was fabricated on a commercial edge-emitting semiconductor laser as the light source. The emission patterns are in agreement with theoretical simulation of such structures. A 90 nm × 70 nm full-width-half-maximum spot size was measured and is comparable to the ridge width of the aperture.

ACKNOWLEDGEMENTS

I would like to express my great thanks to Professor Gilbert Walker. He has been a great advisor during my whole graduate studies. I have been deeply impressed with his knowledge and great enthusiasm toward scientific research and education. I am very thankful for his understanding of my family issues and leading me in my research scientist carrier. I believe that the experience in his group will be invaluable in my career as a research scientist because I have learned many techniques, knowledge and problem-solving skills. Thanks are extended to Professors Waldeck, Amemiya, Levy, Yates, and Bourguet for serving on my committee and for their assistance towards my education.

I would like to thank my collaborators from Carnegie Mellon University, Dr. Chen, Prof. Bain, and Prof. Schlesinger. The second part of my dissertation was conducted in collaboration with them. I have learned a lot during this work and our discussions.

I would like to express my gratitude to all of the present and former members of the Walker group. We shared great times and hard times together as members of an excellent research group. I believe that all of us have worked hard to overcome the hurdles and will have a bright future.

I would like to thank the University of Pittsburgh for giving me the opportunity to study here and for its financial support. I also would like to acknowledge a Mellon Doctoral Fellowship for its financial support.

Finally, I would like to thank my family for their continuous support and, especially, my husband for all his help and encouragement while I was working hard to overcome the difficulties I have encountered during my Ph. D. studies. I dedicate this thesis to my son.

TABLE OF CONTENTS

ABSTRACT iii
ACKNOWLEDGEMENTS v
TABLE OF CONTENTS vi
LIST OF FIGURES viii
1. INTRODUCTION 1
1.1. Methodology 2
1.2. Signal enhancement and polarizability of the tip-sample system in NSOM 4
1.3. Chemical sensitivity of NSOM 6
1.4. Artifact-free near-field signal 9
1.5. High output power in aperture probe NSOM 12
1.6. Conclusions 13
BIBLIOGRAPHY 14
2. ENHANCEMENT OF THE WEAK SCATTERED SIGNAL IN APERTURELESS NEAR-FIELD SCANNING INFRARED MICROSCOPY 19
2.1. Introduction 19
2.2. Experimental details 20
2.3. Homodyne detection of near-field signal 22
2.4. Polarizability of the tip-sample system and magnitude of the detected signal 28
BIBLIOGRAPHY 32
3. MONOLAYER-SENSITIVE INFRARED IMAGING OF DNA STRIPES USING APERTULESS NEAR-FIELD MICROSCOPY 34
3.1. Introduction 34
3.2. Experimental details 35
3.3. Distance dependence of the near-field signal 37
3.4. Submonolayer chemical sensitivity of the near-field apparatus 39
3.5. Conclusions 44
BIBLIOGRAPHY 45
4. FIELD ENHANCEMENT IN VERY SMALL APERTURE LASERS STUDIED BY APERTURELESS NEAR-FIELD MICROSCOPY 47
4.1. Introduction 47
4.2. Experimental details 48
4.3. Dispersion of aluminum surface plasmons 49
4.4. Interference of surface plasmons with an optical field 51
4.5. Influence of the aperture orientation on a field enhancement in optical waveguide 55
BIBLIOGRAPHY 58
5. IMAGING OF OPTICAL FIELD CONFINEMENT IN RIDGE WAVEGUIDES FABRICATED ON VERY-SMALL-APERTURE LASERS 60

5.1. Introduction 60
5.2. C aperture design and FDTD simulations 63
5.3. Optical near-field emission from very small C aperture laser 64
BIBLIOGRAPHY 69
6. CONCLUDING REMARKS 70
BIBLIOGRAPHY 73

LIST OF FIGURES

Figure 1-1 Schematic representation of an apertureless near-field microscope. The laser light is focused onto the end of the probe oscillating near the sample's surface, and the back-scattered radiation from the tip-sample system is focused by means of far-field optics onto the detector's window. Lock-in detection is used to collect the near-field signal at the harmonics of cantilever's oscillation frequency. 3

Figure 1-2 (a) Topography of polymer film sample prepared by spin casting of polystyrene-polydimethylsiloxane diblock polymer on a gold-coated microscope coverslip. (b) The image of near-field infrared signal collected simultaneously with the topography of the sample in constant gap mode. The incident radiation at 982 cm^{-1} was used to illuminate the sample. (c) Infrared signal image created by interpolation of maps of near-field signal collected at various tip-sample gap values to a plane above the sample surface. The contrast on topographic structures is removed; and the residual differential signal on the edges is remaining probably due to a slight drift in the images used for interpolation. 9

Figure 2-1 Schematic representation of the apertureless near-field infrared microscope. The back-scattered light, E_{sc}, is modulated by the oscillating tip. The piezo driver adjusts the relative phase of the homodyning reference field, E_r, that interferes at the detector with the light back-scattered by the probe. The dominant AC contribution to the homodyned intensity at $2\langle E_{sc}E_r\rangle$ is detected using a lock-in amplifier. 21

Figure 2-2 The dependence of the near-field signal on displacement of the partial reflector. Squares represent the data points; solid line represents the fit, whose functional form is the absolute value of cosine of the displacement. 24

Figure 2-3 The amplitude of scattered near-field signal at 2Ω *vs.* (a) the amplitude of dc component, (b) the square root of the amplitude of dc component. Solid lines represent a linear fit to the data points. 25

Figure 2-4 Panel (a) shows the amplitude of cantilever oscillation *vs.* the separation from the sample's surface. Panel (b) shows the amplitude of the scattered near-field signal demodulated at twice the frequency of cantilever oscillation *vs.* tip-sample separation for different intensities of the reference beam. The smallest two signals were obtained without a reference beam. The signal represented by the dashed line was collected when the apparatus was not tuned well. Panel (c) shows the height image of Si deposited onto a gold substrate. The bare gold may be seen as the dark, low-lying, central stripe. Panel (d) shows the apertureless near field infrared image collected in two ways: in the top portion shows the signal collected without benefit of homodyne amplification; in the bottom portion of the figure, beginning at a point indicated by the arrow, the signal was collected with homodyne amplification. The portion of the figure below the arrow is much clearer and exhibits signal that is completely missing in the upper portion. This image demonstrates the value of homodyne amplification for infrared near field microscopy. 26

Figure 2-5 Top panel shows the fit of the one scattering sphere model for the near-field signal. In the model, the sphere oscillates above the surface. The bottom panel shows the fit error. 29
Figure 2-6 The top panel shows the normalized near-field signal-distance dependence (dots) and curves calculated according to the model described in the text (solid lines). The bottom panel shows the fit error..... 30
Figure 3-1 Schematic of the apertureless near-field infrared microscope. 36
Figure 3-2 The top panel shows how the amplitude of the vertical probe oscillation depends on the separation from the surface. The bottom panel shows IR signals demodulated at the frequency of the probe oscillation (f) and twice the oscillation frequency (2f). The interferometric feature present in the f-signal is missing from the 2f-signal..... 39
Figure 3-3 The image on the left shows the topography of the striped DNA- hexadecanethiol sample; the image on the right shows the *2f* infrared signal. The 10 μm stripe pattern can be easily seen in the IR signal image; DNA regions are darker than alkanethiol regions. Several height features that are discernable in the topographic image are not coupled to IR signal. Graphs below each image show the projection of the signal from a 7.5 μm wide area onto a line perpendicular to the linear pattern, as indicated in the corresponding images. .. 40
Figure 3-4 The graph shows the far-field IR absorption of a DNA monolayer grafted onto a gold substrate, in the spectral region of phosphate absorption band (dotted line). The figure also shows the result of averaging the near-field IR images at different wavelengths (triangle symbols)..... 42
Figure 4-1 Geometric relations of the apertureless NSOM components for the imaging of VSAL. 49
Figure 4-2 Dispersion diagram of surface plasmons generated at Al/Si_3N_4 surface. 51
Figure 4-3 (a) Topographic image of the aperture and its surrounding. The dimensions of the aperture were 400 nm x 100 nm. (b), (c) Near-field signals in and near the aperture. The aperture was rotated 90 degrees prior to collecting image (c). The scan area of the images was 1500 nm x 1500 nm. Plot (d) presents a cross section (dotted line) made in image (c) and a fit (solid line) made according to the surface plasmon point-source model. 52
Figure 4-4 Near-field signals collected in and near the aperture shown in Figure 4-3 using external detector. The aperture was rotated 90 degrees prior to collecting image (b). The external detector was not rotated with the aperture. 54
Figure 4-5 (a) Topographic image of three apertures made on Al coated laser diode. (b) Near-field signal collected in the vicinity of the apertures using integrated photodetectors. Image scan area is 2500 nm x 2500 nm. (c) Section line indicated in (b) by dashed line..... 55
Figure 5-1 A ridge waveguide structure (C aperture) that can have high power throughput..... 61
Figure 5-2 (a) Detailed geometry of a designed ridge waveguide structure, (b) FIB image of such a ridge waveguide fabricated on VSAL (arrow indicating active layer position); (c) and (d) are FDTD simulations of this ridge waveguide showing the E_x field structure (the dominant component) and total field *E* distribution at the exit plane of the aperture..... 63
Figure 5-3 Detailed geometric relations of the apertureless NSOM components for ridge waveguide structure imaging. The structure is fabricated along the active layer..... 64
Figure 5-4 Observation of optical field confinement in the ridge waveguide: (a) Near-field image at *1f* detection; (b) near-field image at *2f* detection, (c) and (d) are the height images with optical intensity contours for *1f* and *2f*. Spot size confinement effect is clearly indicated... 66

1. INTRODUCTION

It is important to be able to see objects with the highest possible magnification in many science areas such as chemistry and biology. The resolution in traditional optical techniques is limited by the diffraction limit. Other techniques, such as atomic force microscopy (AFM), scanning electron microscopy (SEM), or scanning tunneling microscopy (STM), have been developed to view the samples with high resolution. But these techniques miss chemical properties of the sample. The limitation in optics has been broken by developing a new tool, known as the scanning near-field optical microscope (SNOM). It allows one to overcome the diffraction limit in conventional microscopy and to obtain the chemical information about the samples with resolution on the nanometer scale.[1] The principle of operation of a near-field microscope is based on the detection of the evanescent waves, which contain information about chemical properties of an object. SNOM can be used to study a variety of samples from semiconductors to polymers and biological materials in the spectral range from ultraviolet radiation to radio waves.[2] The first near-field microscope was proposed by Synge in 1928, who suggested imaging a sample using a nanoaperture illuminated by the light and brought to the sample surface as close as only few nanometers. His work was the basis of all techniques that use an aperture as a nanosource or a nanocollector of the light. Currently the achievable resolution is $\lambda/20$ in the visible region[2] and $\lambda/10$ in the infrared region[3] for the aperture probe technique. An alternative technique was proposed by Wessel in 1985, which is called apertureless, or scattering-type scanning near-field microscopy. The idea of this method is to perturb electromagnetic waves localized at the surface

of the sample so that the decaying components of the field will propagate to a remote detector.[1] This approach has been used to obtain maps of local scattered field and fluorescence beneath the probe on variety of samples.[4-14] Apertureless imaging usually provides better resolution, than aperture probe technique. It is possible to achieve λ /100 in visible region[4-6] and λ /300 in infrared.[15, 16]

1.1. Methodology

The scanning capabilities of a commercial atomic force microscope are often used in near-field microscope. There are two types of near-field techniques: aperture and apertureless probe technique; the main difference between them is the design of the probe which is used to scan the sample. Research groups that are using aperture technique now usually employ a metal-coated optical fiber illuminated by the laser light to scan the sample.[2, 17, 18] Such near-field probes can be made from single-mode zirconium fluoride glass fiber to be used for infrared imaging.[18] The cutoff diameter of a fiber is proportional to the wavelength and this significantly limits spatial resolution in the infrared. The procedure of tapering the end of the fiber is usually used to make the end of the fiber of subwavelength radius. It can be done using both "heat and pull" method[19] and a chemical etching scheme.[20, 21] The apertureless probe technique usually employs a metallic, semiconductor, or dielectric probe as a local scatterer of electromagnetic radiation in the vicinity of a sample surface. Researchers widely use commercially available probes, or specially shaped probes can be designed in the laboratory.[22,23] The radius of curvature of commercial probe can be as small as 35 nm.[24] Although, the apertureless probes provide better resolution than apertured probes, the use of apertured probes provides better the signal-to-noise

ratio in near-field images. This is because the sides of metal probes also scatter the light, which is not specific to the sample surface. A small metal particle attached to the end of the probe tip can be used to reduce unwanted scattering in the apertureless probe technique.[23]

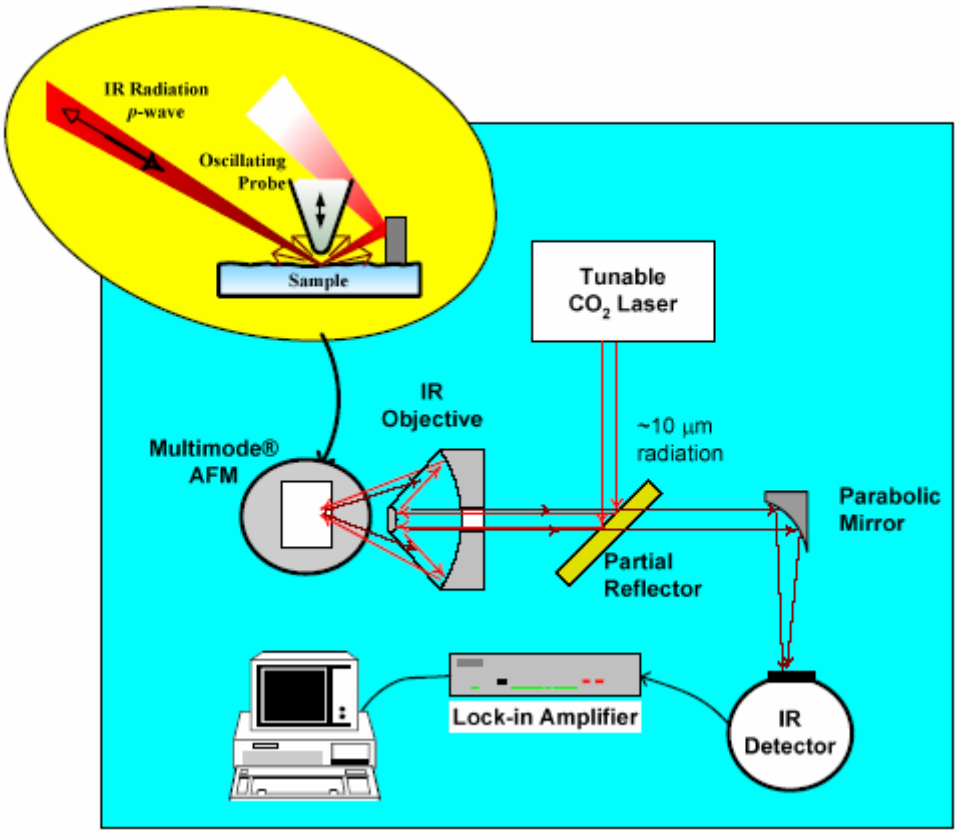

Figure 1-1 Schematic representation of an apertureless near-field microscope. The laser light is focused onto the end of the probe oscillating near the sample's surface, and the back-scattered radiation from the tip-sample system is focused by means of far-field optics onto the detector's window. Lock-in detection is used to collect the near-field signal at the harmonics of cantilever's oscillation frequency.

In a typical apertureless near-field microscope the light from a laser is focused onto the end of the probe, and the scattered light, converted into the propagated radiation by the probe, is

focused onto the remote detector (see Figure 1-1). Oscillating the probe near its resonance frequency is often used in the detection of the near-field signal,[9, 13] which allows one to use the benefits of lock-in sensitive detection in near-field microscopy. The ac-mode operation of the SNOM is shown to be effective for background noise reduction in collection of near-field signal.[9] But, it has been noted that the signal collected at the frequency of cantilever oscillation still might have a significant component which is not specific to the sample.[24] The interference of the radiation from different parts of the cantilever can contribute to the signal.[25] Detection of the scattered signal at the harmonics of the cantilever oscillation frequency provides a convenient way to collect surface-specific signal.[26-28]

1.2. Signal enhancement and polarizability of the tip-sample system in NSOM

The scattered signal collected at twice the frequency of cantilever oscillation is very weak. It has been shown, that near-field signal can be enhanced by using either homodyne detection,[29-32] or heterodyne detection.[33, 34] Both interferometric methods involve introducing a reference field whose optical frequency is the same (homodyne detection), or slightly shifted (heterodyne detection) from the frequency of incident light. Enhancement of the weak scattered signal in apertureless NSOM using homodyne detection will be discussed in details in Chapter 2. It also includes the disscution that near-field signal can be self-homodyned and its behavior depends dramatically on the tip environment and the position of the probe with respect to the sample surface.[31, 35] Self-homodyning effect must be taken into account for a correct interpretation of near-field images. But, the use of external interferometer permits one to control the interferometric effect.

To understand the origin of chemical contrast in near-field microscopy a coupled-dipoles model[4] has been used.[28, 31, 36] It predicts a nonlinear polarizability modulation of the tip and the sample upon tip-sample separation (Equation 1). Knoll and Keilmann[36] suggested that one should consider the electrical dipole moment of the tip, which has a shape simplified to a sphere, along with its image dipole in the sample. The local field interaction of the spherical tip of radius a and dielectric constant ε_t with a sample, considered as a halfspace with dielectric constant ε_s, upon tip-sample separation d, can be described by the effective polarizability:

$$\alpha_{\perp}^{eff} = \frac{\alpha(1+\beta)}{1-\frac{\alpha\beta}{16\pi(a+d)^3}}, \tag{1}$$

where $\alpha = 4\pi a^3 \frac{\varepsilon_t - 1}{\varepsilon_t + 2}$ and $\beta = \frac{\varepsilon_s - 1}{\varepsilon_s + 1}$.

By applying Mie theory, the scattering and absorbing cross-sections of the near-field tip (considered as a gold sphere) on the gold and silicon samples have been calculated.[28] The result indicated a steep increase of scattering cross-sections at small probe-sample distances. These results agree with the experiments conducted by Knoll and Keilmann.[28] But this model does not explain well the long distance interactions between the tip and the sample.[31] This can be expected since the probe is not a nanometer-sized sphere but extends significantly further away from the surface. Chapter 2 presents the results of the effective polarizability calculations which take into account a signal scattered from the upper part of the tip.

1.3. Chemical sensitivity of NSOM

Infrared near-field microscope combines nanoscale resolution of scanning microscope with the infrared spectroscopy. Although, fluorescence near-field microscopy has been used to image biological materials,[14, 37] only few attempts to identify the chemical composition of a sample with infrared sensitivity have been conducted.[13, 16, 18, 24, 25, 32, 38] Chapter 3 presents infrared near-field microscopy study of a sample with alternative stripes of DNA and alkanthiol submonolayers. It will be shown that submonolayer chemical sensitivity can be achieved using infrared near-field microscopy.

Other groups also obtained chemical sensitivity of near-field apparatus on different samples. Taubner *et al.*[32] used homodyne detection scheme to obtain infrared near-field map of a sample containing three different materials, Au, Si, and polystyrene. They presented an optical image, collected with 9.7 μm incident light, that clearly distinguishes different components of a sample. The comparison of optical image with the topography of this sample shows that topography alone was not sufficient to distinguish between different materials. The optical resolution of better than 20 nm has been demonstrated in this infrared near-field imaging. Taubner *et al.* have also predicted theoretically and have shown experimentally that the contrast in the near-field images arises only from the dielectric properties of these components.

The super-resolution of infrared near-field microscopy has been used to identify the decomposition of cholesteryl oleate to cholesterol and oleic acids after illumination of the sample with infrared light.[38] The near-field images of the sample have been collected at two different wavelengths, 5.75 and 5.3 μm, which correspond to in and out of resonance with the absorption band of the ester bonds, accordingly. Masaki *et al.* have shown that the difference in the contrast

between these two images arises from two factors: artifacts due to scattering and IR absorption due to the molecules in the film. They have used a 2 μm apertured cantilever probe to successfully identify areas of molecular change in cholesteryl oleate well beyond the diffraction limit.

Raman scattering is also known as a powerful tool for direct observation of molecular vibrations. Near-field Raman imaging can be used for *in situ* chemical analysis of objects on nanometer scale. Hayazawa *et al.* have applied tip-enhanced Raman microscope to study molecular vibrations in organic molecules.[39-42] They have shown that the near-field Raman spectra reveal new vibrations that can not be detected by conventional surface enhanced Raman spectroscopy. Several characteristic Raman peaks of polycrystalline Rhodamine6G dyes[39, 40] and adenine molecules[42] were enhanced by the presence of near-field tip and became visible with a nanometer resolution. The lateral resolution of 30 nm obtained in near-field Raman imaging[40] and the possibility to detect weak Raman scattering from a nanometer region provides a possibility to study single molecule vibrations. Hayazawa *et al.* have already obtained structural analysis of an individual single-wall carbon nanotube using the tip-enhanced near-field Raman spectroscopy.[42]

Single-wall carbon nanotubes (SWNTs) are very popular among the researchers due to their potential nanotechnological applications. Studies conducted by Hartschuh *et al.*[43, 44] have also showed that the individual SWNTs can be detected by near-field Raman microscopy with a spatial resolution better than 30 nm. Near-field Raman image provided by Hartschuh and co-workers clearly identifies spatially separated SWNTs and it does not show any signals from other topographic features formed on the sample surface due to condensation of water. Hartschuh *et al.*[43] have also demonstrated the confinement of near-field Raman signal while collected as a

function of tip-SWNT distance. The decay length of 11 nm was obtained from the fit of scattered signal distance dependence, which clearly indicates near-field contribution to the signal. The evidences provided above strongly prove the chemical specificity of near-field Raman microscopy.

De Groot *et al.*[45] and De Serio *et al.*[46] have also contributed to the developing of chemically sensitive optical technique based on the near-field spectroscopy. Recently, they have used the high spatial resolution capability of near-field Raman spectroscopy to study the interface between two immiscible liquids (*p*-xylene and ethylene glycol).[46] Changes in Raman spectra due to the influence of the phase boundary have been detected with a spatial resolution of 1 μm. It has been noticed that the influence of the phase boundary on the Raman bands of *p*-xylene near the interface extends as far as 10 μm from the liquid-liquid interface. It has been also demonstrated that the uncoated tips used in the experiments add more unwanted background scattering to the near-field signal in liquid, then the metal-coated tips.

One of the future directions in the near-field chemical imaging will be modification of the existing near-field microscope to enable imaging in liquid. While visualizing and studying chemical properties of living cells and biomolecules with nanometer scale resolution, achievable in near-field microscopy, is very important, only a few attempts to do so have been made (see references in 47). This is because realistic properties of such objects can only be obtained under physiological conditions, which are usually realized in liquid. The main difficulties to overcome in realizing biological NSOM are the fabrication of the near-field probes that will efficiently transmit or reflect light in liquid, and the ability to control distance between the tip and soft sample in liquid.[47] While all near-field studies in liquid represent fluorescence imaging, the

infrared imaging has a great importance for studying biological sample under physiological conditions. The infrared near-field microscopy in liquid is yet to be developed.

1.4. Artifact-free near-field signal

It is important to be aware of the artifacts that can arise in the near-field optical microscopy. Several articles discuss the problems and their possible solutions in obtaining "true" near-field signal.[24, 29, 48-50] The most common artifact in the near-field microscopy is the crosstalk between the near-field images and the topography of the sample. The near-field signal changes rapidly with the distance from the sample, and the motion of the tip perpendicular to the sample surface due to gap-width control, which is often used during scanning the sample, contributes to the variations in the near-field signal, which are not caused by the optical properties of the material.

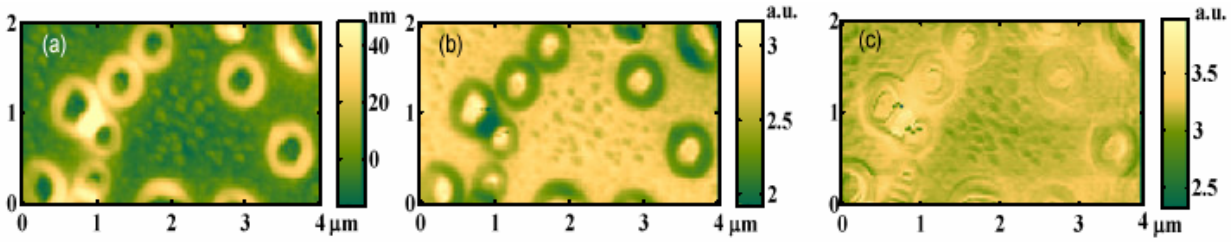

Figure 1-2 (a) Topography of polymer film sample prepared by spin casting of polystyrene-polydimethylsiloxane diblock polymer on a gold-coated microscope coverslip. (b) The image of near-field infrared signal collected simultaneously with the topography of the sample in constant gap mode. The incident radiation at 982 cm^{-1} was used to illuminate the sample. (c) Infrared signal image created by interpolation of maps of near-field signal collected at various tip-sample gap values to a plane above the sample surface. The contrast on topographic structures is removed; and the residual differential signal on the edges is remaining probably due to a slight drift in the images used for interpolation.

The z-motion artifact generates features in the optical image that are strongly correlated with the structures in the topographic image[48] (see also Figure 1-2a, b). The presence of this artifact is not obvious because of the origin of the formation of the optical images. Such correlation can be expected due to the correlation of sample topography with its optical structure and can be misleading in the interpretation of the near-field signal.

Although the constant gap mode allows the inspection of morphologically complex samples, the constant height mode, where the tip moves only laterally over the sample surface, is a good way to obtain purely optical near-field images.[49] Operation in constant height mode requires using flat surfaces, and topographic image obtained in constant gap mode is needed in order to identify topographical contributions to the optical signal. Another way to minimize the influence of topography on the near-field signal is demonstrated in reference 24. Akhremitchev *et al.* interpolated the near-field images collected at different probe-sample gap values to a plane above the sample surface. As a result of a such procedure, the strong near-field signal above the tall sample features almost completely disappear, allowing one to see less intense variations in the near-field signal in the flat area of the sample (Figure 1-2c), that are believed to be due to local variations of pure optical properties of the sample. Although it is not always convenient, working with a very flat sample in constant gap mode will significantly reduce the topographic artifact. In all other cases Hecht *et al.*[48] suggested relying on the following observations in obtaining artifact-free near-field signal:

- Topographic and near-field images are highly uncorrelated.
- Correlated structures are displaced by the same amount.
- The resolutions of near-field and topography images are different.

There are other ways that may help reduce the topographic contribution in the near-field signal. An alternative to the operation in constant height mode has been suggested by Azoulay et al.[29] They have shown that optical images collected by means of homodyne detection exhibit "true" near-field optical contrast, where the topographic artifact is greatly reduced. The use of the second harmonic detection in collecting near-field signal has also been applied to eliminate z-motion artifact from optical images.[49]

The probe itself may be the source of the artifacts in near-field imaging. The asymmetry of the tip may lead to the changes in the near-field signal that do not reflect optical properties of the sample.[50] The direction and position of the incident beam provide a great influence on the near-field images.[51] The far-field interference of the light may be observed in the images collected using reflection-mode near-field microscope. This pattern appears because the large portion of the cantilever is illuminated giving rise to the interference of the reflected light from the cantilever in far-field. It is possible to reduce this artifact by lowering the illumination beam to avoid the cantilever illumination.[51] It has been shown that the total internal reflection illumination mode is more suitable for near-field imaging in order to avoid the far-field diffraction caused by the tip.[51] The geometry of the tip also influences the local optical field enhancement which can occur at the end of the metallic tip.[51] The spatial confinement in near-field images depends on the cone angle of the tip. It has been observed by Bachelot *et al.* that a wide-angle cone gives rise to the near-field signal collected under the tip and produces a wider field distribution in the near-field images than a narrow cone. On the other hand, one should take into the account the radius of curvature of the tip while analyzing the near-field images. It has been shown that with a large curvature of the tip the intensity beneath the tip is neither enhanced

nor spatially confined.[51] The optimization of the tip geometry[22] will allow obtaining optimal field enhancement and a better spatial resolution in near-field microscopy.

1.5. High output power in aperture probe NSOM

Until this, point of this chapter has been devoted to apertureless near-field microscopy. A way to obtain high power output in apertured probe NSOM will be discussed in Chapters 4 and 5. Here is a brief introduction.

Fabrication of a very small aperture in an opaque metallic film is one effective method to obtain a near-field nanoscale light source. Its integration with a semiconductor laser diode which is called the very small aperture laser (VSAL) is more attractive in various fields such as near-field scanning optical microscopy, near-field optical data storage, nano-photolithography and near-field spectroscopy.[52] The near-field nanoscale light source should not only have an ultrahigh resolution light spot in nanometer scale, but also should have sufficient output power for practical applications.

Any laser diode can accept the very small aperture design. A focused ion beam simply etches an aperture of the desired size into a metal coating deposited on the front facet of the diode.[53] The researchers have produced the devices with rectangular apertures of 50 to 400 nm on a side.[54] The lasers display an output 10^4 times that of tapered, metal-coated optical fiber probes, the most common light source for near-field scanning microscopy.[52] A higher-power light source may increase the signal-to-noise ratios and data rates of current applications as well as lead to the development of compact near-field microscopes. The mechanisms of the resonant transmission of the subwavelength apertures positioned over the laser diodes will be discussed in Chapter 4.

Square and circular apertures suffer from very low transmission efficiency when the aperture dimensions are much smaller than one wavelength. Recently, a "C"-shaped aperture was discovered by Shi *et al.* with FDTD simulation to have about 1000 times higher power transmission than square apertures with comparable near-field spatial resolution.[55] Very small C-shaped aperture lasers promise to have both very small near-field spot size and sufficiently high power density for optical recording.[56] Chapter 5 will present the images of near-field optical emission collected from very small C-shape aperture laser.

1.6. Conclusions

The development of several imaging techniques, including constant height imaging, detection of the scattered signal at higher harmonics of the tip motion, and enhancing weak scattered signal using homodyne detection have enabled significant advances in near-field scanning optical microscopy. Submonolayer chemical sensitivity and spatial resolution of better than 25 nm in infrared near-field imaging have been reported. The rational design of probe shape and composition will further improve spatial resolution and field enhancement under the tip. The resolution of aperture probe NSOM can be improved by using VSALs as the nanoscale light sources. Further development of near-field microscopy to enable imaging in liquid will bring new possibilities for biological applications.

BIBLIOGRAPHY

1. Courjon, D.; Bainier, C. Near field microscopy and near field optics. *Rep. Prog. Phys.* **1994**, *57*, 989-1028.

2. Hecht, B.; Sick, B.; Wild, U. P.; Deckerd, V.; Zenobi, R.; Martin, O. J. F.; Pohl, D. W. Scanning near-field optical microscopy with aperture probes: Fundamentals and applications. *J. Chem. Phys.* **2000**, *112*, 7761-7774.

3. Dragnea, B.; Preusser, J.; Schade, W.; Leone, S. R.; Hinsberg, W. D. Transmission near-field microscope for infrared chemical imaging. *J. Appl. Phys.* **1999**, *86*, 2795-2799.

4. Zenhausern, F.; Martin, Y.; Wickramasinghe, H. K. Scanning interferometric apertureless microscopy: optical imaging at 10 angstrom resolution. *Science* **1995**, *269*, 1083-1085.

5. Hamann, H. F.; Gallagher, A.; Nesbitt, D. J. Enhanced sensitivity near-field scanning optical microscopy at high spatial resolution. *Appl. Phys. Lett.* **1998**, *73*, 1469-1471.

6. Hubert, C.; Levy, J. Nanometer-scale imaging of domains in ferroelectric thin films using apertureless near-field scanning optical microscopy. *Appl. Phys. Lett.* **1998**, *73*, 3229-3231.

7. Adam, P. M.; Royer, P.; Laddada, R.; Bijeon, J. L. Polarization contrast with an apertureless near-field optical microscope. *Ultramicroscopy* **1998**, *71*, 327-331.

8. Yamaguchi, M.; Sasaki, Y.; Sasaki, H.; Konada, T.; Horikawa, Y.; Ebina, A.; Umezawa, T.; Horiguchi, T. Imaging of optical disc using reflection-mode scattering-type scanning near-field optical microscopy *J. Microsc. (Oxford)* **1999**, *194*, 552-557.

9. Sasaki, H.; Sasaki, Y. Imaging of refractive index change by the reflection-mode scattering-type scanning near-field optical microscope: Simulation and observations. *J. Appl. Phys.* **1999**, *85*, 2026-2030.

10. Azoulay, J.; Debarre, A.; Richard, A.; Tchenio, P. Field enhancement and apertureless near-field optical spectroscopy of single molecules. *J. Microsc. (Oxford)* **1999**, *194*, 486-490.

11. Sanchez, E. J.; Novotny, L.; Xie, X. S. Near-field fluorescence microscopy based on two-photon excitation with metal tips. *Phys. Rev. Lett.* **1999**, *82*, 4014-4017.

12. Hillenbrand, R.; Keillmann, F. Material specific mapping of metal/semiconductor/dielectric nanosystems at 10 nm resolution by backscattering near-field optical microscopy. *Appl. Phys. Lett.* **2002**, *80*, 25-27.

13. Lahrech, A.; Bachelot, R.; Gleyzes, P.; Boccara, A. C. Infrared-reflection-mode near-field microscopy using an apertureless probe with a resolution of λ/600. *Opt. Lett.* **1996**, *21*, 1315-1317.

14. Hausmann, M.; Liebe, B.; Perner, B.; Jerratsch, M.; Greulich, K.-O.; Scherthan, H. Imaging of human meiotic chromosomes by scanning near-field optical microscopy (SNOM). *Micron* **2003**, *34*, 441-447.

15. Lahrech, A.; Bachelot, R.; Gleyzes, P.; Boccara, A. C. Infrared near-field imaging of implanted semiconductors: Evidence of a pure dielectric contrast. *Appl. Phys. Lett.* **1997**, *71*, 575-577.

16. Knoll, B.; Keilmann, F. Mid-infrared scanning near-field optical microscope resolves 30 nm. *J. Microsc. (Oxford)* **1999**, *194*, 512-515.

17. Dunn, R. C. Near-field scanning optical microscopy. *Chem. Rev.* **1999**, *99*, 2891-2927.

18. Michaels, C. A.; Stranick, S. J.; Richter, L. J.; Cavanagh, R. R. Scanning near-field infrared microscopy and spectroscopy with a broadband laser source. *J. Appl. Phys.* **2000**, *88*, 4832-4839.

19. Valaskovic, G. A.; Holton, M.; Morrison, G. H. Parameter control, characterization, and optimization in the fabrication of optical fiber near-field probes. *Appl. Opt.* **1995**, *34*, 1215-1228.

20. Hoffmann, P.; Dutoit, B.; Salanthé, R.-P. Comparison of mechanically drawn and protection layer chemically etched optical fiber tips. *Ultramicroscopy* **1995**, *61*, 165-170.

21. Unger, M. A.; Kossakovski, D. A.; Kongovi, R.; Beauchamp, J. L.; Baldeschwieler, J. D.; Palanker, D. V. Etched chalcogenide fibers for near-field infrared scanning microscopy. *Rev. Sci. Instrum.* **1998**, *69*, 2988-2993.

22. Krug II, J. T.; Sanchez, E. J.; Xie, X. S. Design of near-field optical probes with optimal field enhancement by finite difference time domain electromagnetic simulation. *J. Chem. Phys.* **2002**, *116*, 10895-10901.

23. Kawata, Y.; Urahama, S.; Murakami, M.; Iwata, F. The use of capillary force for fabricating probe tips for scattering-type near-field scanning optical microscopes. *Appl. Phys. Lett.* **2003**, *82*, 1598-1600.

24. Akhremitchev, B. B.; Pollack, S.; Walker, G. C. Apertureless scanning near-field infrared microscopy of a rough polymeric surface. *Langmuir* **2001**, *17*, 2774-2781.

25. Akhremitchev, B. B.; Sun, Y.; Stebounova, L.; Walker, G. C. Monolayer-sensitive infrared imaging of DNA stripes using apertureless near-field microscopy. *Langmuir* **2002**, *18*, 5325-5328.

26. Maghelli, N.; Labardi, M.; Patane, S.; Irrera, F.; Allegrini, M. Optical near-field harmonic demodulation in apertureless microscopy. *J. Microsc. (Oxford)* **2001**, *202*, 84-93.

27. Wurtz, G.; Bachelot, R.; Royer, P. Imaging a GaAlAs laser diode in operation using apertureless scanning near-field optical microscopy. *Eur. Phys. J. Appl. Phys.* **1999**, *5*, 269-275.

28. Knoll, B.; Keilmann, F. Enhanced dielectric constant in scattering-type scanning near-field optical microscopy. *Opt. Commun.* **2000**, *182*, 321-328.

29. Azoulay, J.; Debarre, A.; Richard, A.; Tchenio, P. Optical contrast in apertureless microscopy. *Appl. Opt.* **2000**, *39*, 129-134.

30. Bridger, P. M.; McGill, T. C. Observation of nanometer-scale optical property discrimination by use of a near-field scanning apertureless microscope. *Opt. Lett.* **1999**, *24*, 1005-1007.

31. Stebounova, L.; Akhremitchev, B. B.; Walker, G. C. Enhancement of the weak scattered signal in apertureless near-field scanning infrared microscopy. *Rev. Sci. Insrumt.* **2003**, *74*, 3670-3674.

32. Taubner, T.; Hillenbrand, R.; Keilmann, F. Performance of visible and mid-infrared scattering-type near-field optical microscopes. *J. Microsc. (Oxford)* **2003**, *210*, 311-314.

33. Hillenbrand, R.; Keilmann, F. Complex optical constants on a subwavelength scale. *Phys. Rev. Lett.* **2000**, *85*, 3029-3032.

34. Sasaki, Y.; Sasaki, H. Heterodyne detection for the extraction of the probe-scattering signal in scattering-type scanning near-field optical microscope. *Jpn. J. Appl. Phys.* **2000**, *39*, L321-L323.

35. Aubert, S.; Bruyant, A.; Blaize, S.; Bachelot, R.; Lerondel, G.; Hudlet, S.; Royer, P. Analysis of the interferometric effect of the background light in apertureless scanning near-field optical microscopy. *J. Opt. Soc. Am. B* **2003**, *20*, 2117-2124.

36. Knoll, B.; Keilmann, F. Near-field probing of vibrational absorption for chemical microscopy. *Nature* **1999**, *399*, 134-137.

37. De Lange, F.; Cambi, A.; Huijbens, R.; De Bakker, B.; Rensen, W.; Garcia-Parajo, M.; van Hulst, N.; Figdor, C. G. Cell biology beyond the diffraction limit: near-field scanning optical microscopy. *J. Cell Sci.* **2001**, *114*, 4153-4160.

38. Masaki, T.; Goto, K.; Inouye, Y.; Kawata, S. Near-field infrared imaging of molecular changes in cholesteryl oleate by free electron laser infrared ablation. *J. Appl. Phys.* **2004**, *95*, 334-338.

39. Hayazawa, N.; Inouye, Y.; Sekkat, Z.; Kawata, S. Near-field Raman scattering enhanced by a metallized tip. *Chem. Phys. Lett.* **2001**, *335*, 369-374.

40. Hayazawa, N.; Inouye, Y.; Sekkat, Z.; Kawata, S. Near-field imaging of organic molecules by an apertureless metallic probe scanning optical microscope. *J. Chem. Phys.* **2002**, *117*, 1299-1301.

41. Hayazawa, N.; Tarun, A.; Inouye, Y.; Kawata, S. Near-field enhanced Raman spectroscopy using side illumination optics. *J. Appl. Phys.* **2002**, *92*, 6983-6986.

42. Hayazawa, N.; Yano, T.; Watanabe, H.; Inouye, Y.; Kawata, S. Detection of an individual single-wall carbon nanotube by tip-enhanced near-field Raman spectroscopy. *Chem. Phys. Lett.* **2003**, *376*, 174-180.

43. Hartschuh, A.; Sanchez, E. J.; Xie, X. S.; Novotny, L. High-resolution near-field Raman microscopy of single-walled carbon nanotubes. *Phys. Rev. Lett.* **2003**, *90*, 095503(1)-095503(4).

44. Hartschuh, A.; Anderson, N.; Novotny, L. Near-field Raman spectroscopy using a sharp metal tip. *J. Microsc. (Oxford)* **2003**, *210*, 234-240.

45. De Groot, P. J.; Postma, G. J.; Melssen, W. J.; Buydens, L. M. C., Deckert, V.; Zenobi, R. Application of principal component analysis to detect outliers and spectral deviations in near-field surface enhanced Raman spectra. *Anal. Chim. Acta* **2001**, *446*, 71-83.

46. De Serio, M.; Bader, A. N.; Heule, M.; Zenobi, R.; Deckert, V. A near-field optical method for probing liquid-liquid interfaces. *Chem. Phys. Lett.* **2003**, *380*, 47-53.

47. Ianoul, A.; Burgos, P.; Lu, Z.; Taylor, R. S.; Johnston, L. J. Phase separation in supported phospholipids bilayers visualized by near-field scanning optical microscopy in aqueous solution. *Langmuir*, **2003**, *19*, 9246-9254.

48. Hecht, B.; Bielefeldt, H.; Inouye, Y.; Pohl, D. W. Novotny, L. Facts and artifacts in near-field optical microscopy. *J. Appl. Phys.* **1997**, *81*, 2492-2498.

49. Labardi, M.; Patane, S.; Allegrini, M. Artifact-free near-field optical imaging by apertureless microscopy. *Appl. Phys. Lett.* **2000**, *77*, 621-623.

50. Palanker, D. V.; Simanovskii, D. M.; Huie, P.; Smith, T. I. On contrast parameters and topographic artifacts in near-field infrared microscopy. *J. Appl. Phys.* **2000**, *88*, 6808-6814.

51. Bachelot, R.; H'Dhili, F.; Barchiesi, D.; Lerondel, G.; Fikri, R.; Royer, P.; Landraud, N.; Peretti, J.; Chaput, F.; Lampel, G.; Boilot, J.-P.; Lahlil, K. Apertureless near-field optical

microscopy: A study of the local tip field enhancement using photosensitive azobenzene-containing films. *J. Appl. Phys.* **2003**, *94*, 2060-2072.

52. Partovi, A.; Peale, D.; Wuttig, M.; Murray, C. A.; Zydzik, G.; Hopkins, L.; Baldwin, K.; Hobson, W. S.; Wynn, J.; Lopata, J.; Dhar, L.; Chichester, R.; Yeh, J. H.-J. High-power laser light source for near-field optics and its application to high-density optical data storage. *Appl. Phys. Lett.* **1999**, *75*, 1515-1517.

53. Chen, F.; Zhai, J.; Stansil, D. D.; Schlesinger, T. E. Fabrication of very small aperture laser (VSAL) from a commercial edge emitting laser. *Jpn. J. Appl. Phys.* **2001**, *40*, 1794-1795.

54. Chen, F.; Stancil, D. D.; Schlesinger, T. E. Aperture shape effect on the performance of very small aperture lasers. *J. Appl. Phys.* **2003**, *93*, 5871-5875.

55. Shi, X.; Thornton, R.; Hesselink, L. Nano-aperture with 1000x power throughput enhancement for very small aperture laser system (VSAL). *Proc. of SPIE* **2001**, *4342*, 320-327.

56. Chen, F.; Itagi, A.; Bain, J. A.; Stancil, D. D.; Schlesinger, T. E.; Stebounova, L.; Walker, G. C.; Akhremitchev, B. B. Imaging of optical field confinement in ridge waveguides fabricated on very-small-aperture laser. *Appl. Phys. Lett.* **2003**, *83*, 3245-3247.

2. ENHANCEMENT OF THE WEAK SCATTERED SIGNAL IN APERTURELESS NEAR-FIELD SCANNING INFRARED MICROSCOPY[§]

An interferometric method is used to enhance the weak scattered signal in apertureless near-field scanning infrared microscopy. The method involves introducing a homodyning reference field, and amplifies the desired signal field by the magnitude of the reference field. This method markedly improves the signal-to-noise ratio of the detected signal, over the non-homodyned experiment. A model for the dependence of the near field signal, as a function of the normal distance of the tip from the surface, is discussed. Application of a model in which the tip is represented by two spherical scatterers, one large and one small, indicates the electromagnetic field enhancement is 90 fold greater at the sharp apex of metallic probe tip.

2.1. Introduction

The highest resolution infrared microscopy is apertureless near-field scanning infrared microscopy (ANSIM). It uses a metallic, semiconductor, or dielectric probe as a scattering site for radiation in the immediate vicinity of the sample surface. Wessel is credited with proposing the apertureless probe technique.[1] The idea of this method is to perturb the electromagnetic field localized at the surface of a sample so that the decaying components of the field will propagate

[§] This work has been published as Stebounova, L.; Akhremitchev, B. B.; Walker, G. C. Enhancement of the weak scattered signal in apertureless near-field scanning infrared microscopy. *Rev. Sci. Insrumt.* **2003**, *74*, 3670-3674.

to a remote detector.[2] The tip is oscillated normal to the surface and scattered light is collected at harmonics of the oscillatory frequency. The spatial resolution obtained by this method can be at least an order of magnitude better than is obtained by the apertured probe technique.[3-8] ANSIM has been reported at a lateral spatial resolution of λ/300 in the infrared,[9] and λ/100 for the analogous measurement in the visible.[10] This work has taken place along with notable developments in apertured near-field methods and other new optical and infrared microscopies.[11-20]

In apertureless near field IR microscopy, the development of several imaging techniques, including constant height imaging, detection of the scattered signal at higher harmonics of the tip motion, heterodyne detection, and homodyne detection,[21-24] in addition to the availability of new IR, tunable sources, have set the stage for significant advances. One of the primary challenges in apertureless near-field microscopy is the detection of the weak scattered field. This paper presents a solution to this problem, which is to homodyne the scattered field using a reference field. This provides a signal enhancement that scales as the reference field amplitude, and also provides significant reduction of the time required to align the apparatus.

2.2. Experimental details

The scanning near-field microscope built in our laboratory (Figure 2-1) is based on a commercial atomic force microscope (MultiMode AFM, Digital Instruments Inc., Santa Barbara, CA). It uses a tunable carbon dioxide laser as the source of infrared light. The infrared light passes through a ZnSe partial (50/50) reflector (II-VI Inc., Saxonburg, PA), and it is focused by means of a reflective objective (0.28 NA, Coherent Inc., Auburn, CA) onto the end of cantilever probe. Both

reflective objective and partial reflector are attached to a XYZ translational stage to assist in focusing the light. The probe is a commercial silicon probe (MikroMasch, Tallinn, Estonia) coated with 25 nm of platinum. The incident light is *p*-polarized light with an ~80° angle of incidence. The spot width is approximately 50 μm, and the radiation power is 20-100 mW. The beam from He-Ne laser co-propagates with infrared beam, and it is used to visualize the path of infrared radiation. Infrared radiation back-scattered by the sample and the probe returns through the same reflective objective and partial reflector.

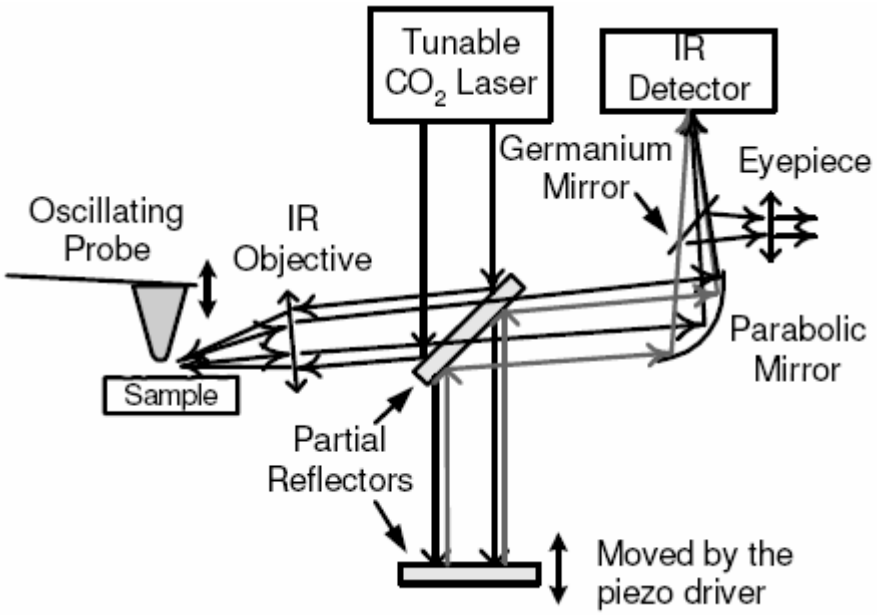

Figure 2-1 Schematic representation of the apertureless near-field infrared microscope. The back-scattered light, E_{sc}, is modulated by the oscillating tip. The piezo driver adjusts the relative phase of the homodyning reference field, E_r, that interferes at the detector with the light back-scattered by the probe. The dominant AC contribution to the homodyned intensity at $2\langle E_{sc}E_r\rangle$ is detected using a lock-in amplifier.

It is focused onto an MCT infrared detector (Graseby Infrared, Orlando, FL) using a paraboloidal mirror (effective focal length 127 mm, Janos Technology Inc., Townshend, VT). The MCT detector is situated on a separate traslational stage in order to adjust its position into the scattered light.

The MCT detector signal contains the nonmodulated background signal (dc component) and the modulated signal at the frequency of cantilever oscillations and its harmonics (ac component). The weak scattered signal from the probe is amplified interferometrically. This optical setup is very similar to a Michelson interferometer. The partial reflector is placed onto a moving stage, which is driven by the piezo driver. The piezo driver has an automated phase feedback control, which is used to maximize the detected signal. The intensity of reference beam was modified by inserting a partial reflector into the reference beam arm of the interferometer.

The ac component was amplified using a lock-in amplifier analyzing at twice the frequency of cantilever oscillation. A gold film (thickness ~20nm) evaporated on a microscope coverslip was used as a substrate. The frequency of the incident light was ~950 cm^{-1}.

2.3. Homodyne detection of near-field signal

The detection of the near-field signal is based on lock-in detection of the signal modulated by an oscillating probe tip at integer multiples of the frequency of the oscillation. This modulation is used to extract the near-field signal from the scattered background. It has been noted that signal modulated at the fundamental frequency (Ω) of cantilever oscillation still contains a large contribution from the signals from different sources that are not surface specific.[20, 25] We use the detection of the near-field signal modulated at the harmonic (2Ω) of the probe oscillation in

order to eliminate the background contribution.[22, 25, 26] In some cases the detection of scattered signal at the harmonics of oscillation frequency is not sufficient to extract truly optical signal. The use of the homodyne or heterodyne detection is employed to remove unwanted signal.[21-24] Our goal is to improve signal-to-noise ratio by amplifying the weak near-field signal collected at second harmonic of the oscillation frequency using homodyne detection.

Since we have an interference of scattered and reference beams, the total intensity of the signal at the detector is

$$I_t = \left\langle (E_{sc} + E_r)^2 \right\rangle = \left\langle E_{sc}{}^2 \right\rangle + \left\langle E_r{}^2 \right\rangle + 2\left\langle E_{sc} E_r \right\rangle, \tag{2}$$

where E_{sc} is the scattered field and E_r is the reference field.

Here is the expression for E_{sc}, which is modulated by the oscillating cantilever:

$$E_{sc} = A_1\left(1 + C_1 \cos(\Omega t) + C_2 \cos(2\Omega t + \Phi)\right)\cos(\omega t + \varphi),$$

where A_1 is the amplitude of the nonmodulated scattered light, C_1 and C_2 are the fractions of first and second harmonics of the demodulated near-field signal, Φ is the relative phase of the second harmonic signal, ω and φ are the frequency and the phase shift of the incident light, Ω is the frequency of cantilever oscillations, and we consider E_r in the form:

$$E_r = A_2 \cos(\omega t),$$

where A_2 is the amplitude of the reference signal, and ω is the frequency of the incident light, then the amplitude of the ac component of the signal at the 2Ω detection frequency is

$$AC = A_1{}^2\left(\frac{C_1{}^2}{4} + C_2\right) + A_1 A_2 C_2 \cos\varphi, \tag{3}$$

and the amplitude of the dc component of the detector signal is

$$DC = \frac{A_2^2}{2} + \frac{A_1^2}{4}(2 + C_1^2 + C_2^2) + A_1 A_2 \cos\varphi \,. \tag{4}$$

Since amplitude A_1 is much less than A_2 and fractions C_1, C_2 are small, we can neglect the first term in equation (3) and second term in equation (4). The phase shift φ between reference and scattered beams is adjusted to maximize the signals using automated phase feedback control. Figure 2-2 shows how the ac component depends on the phase shift.

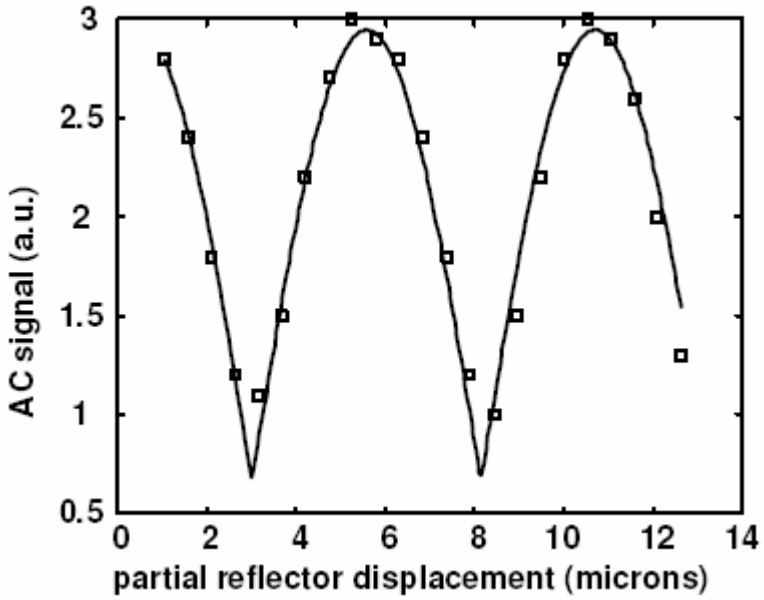

Figure 2-2 The dependence of the near-field signal on displacement of the partial reflector. Squares represent the data points; solid line represents the fit, whose functional form is the absolute value of cosine of the displacement.

The phase feedback uses the lock-in amplifier in order to monitor the deviations of the signal from its maximum position. The relative phase of the reference beam reflector is modulated by oscillating position of the reflector with piezo element at a frequency of 10 Hz and with ~500 nm

peak-to-peak amplitude. The effect of such modulation on the 2Ω component is detected with another lock-in amplifier operating at the frequency of position modulation. The demodulated output is used as a feedback signal of the custom-built piezo driver. The piezo driver moves the reflector in order to zero the feedback signal and hence to maximize the ac signal. Such motion occurs on a time scale of several seconds and it does not affect data collected within one scan line. Slow variations in phase of the reference beam due to, *e.g.,* thermal drift, are compensated. The amplitude of ac signal is proportional to the square root of the amplitude of the interferential dc component:

$$AC \propto \sqrt{DC}\,, \tag{5}$$

where AC is the ac component amplified by homodyne detection and DC is the dc component amplified by homodyne detection dc component.

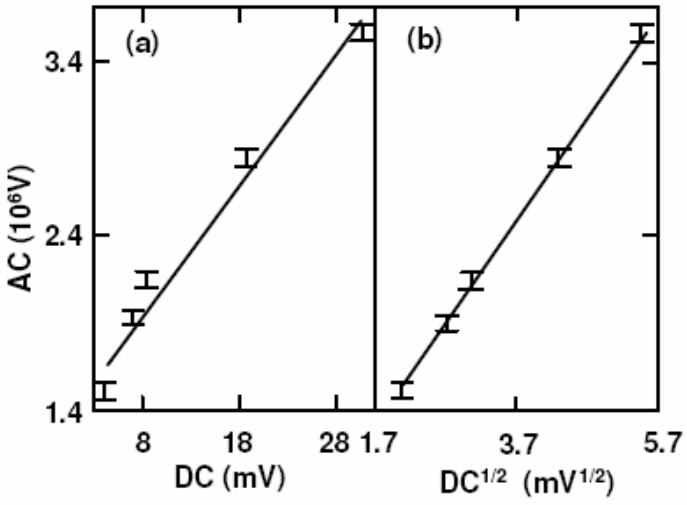

Figure 2-3 The amplitude of scattered near-field signal at 2Ω *vs.* (a) the amplitude of dc component, (b) the square root of the amplitude of dc component. Solid lines represent a linear fit to the data points.

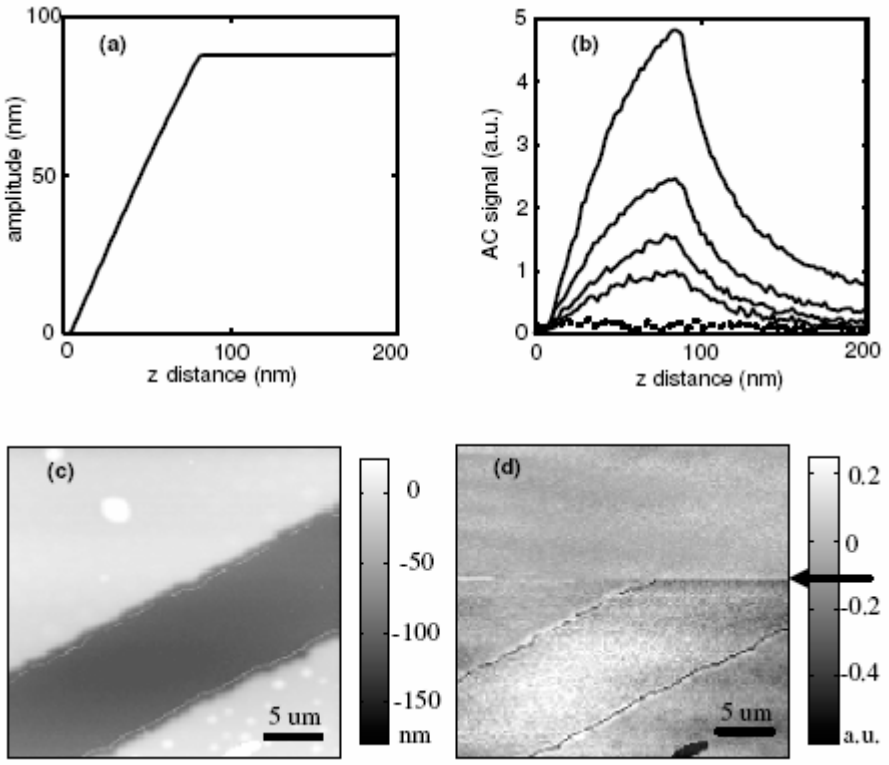

Figure 2-4 Panel (a) shows the amplitude of cantilever oscillation *vs.* the separation from the sample's surface. Panel (b) shows the amplitude of the scattered near-field signal demodulated at twice the frequency of cantilever oscillation *vs.* tip-sample separation for different intensities of the reference beam. The smallest two signals were obtained without a reference beam. The signal represented by the dashed line was collected when the apparatus was not tuned well. Panel (c) shows the height image of Si deposited onto a gold substrate. The bare gold may be seen as the dark, low-lying, central stripe. Panel (d) shows the apertureless near field infrared image collected in two ways: in the top portion shows the signal collected without benefit of homodyne amplification; in the bottom portion of the figure, beginning at a point indicated by the arrow, the signal was collected with homodyne amplification. The portion of the figure below the arrow is much clearer and exhibits signal that is completely missing in the upper portion. This image demonstrates the value of homodyne amplification for infrared near field microscopy.

We collected near-field signal at five different intensities of the reference signal. Both components were normalized by the intensity of the incident light. Data were collected at twice the frequency of the cantilever oscillations. Panel (a) on Figure 2-3 shows the *AC vs. DC*

dependence. The linear fit does not correlate well with the data points. Panel (b) shows a very good correlation between the data and the linear fit.

The distance dependencies of AC signals are presented in Figure 2-4. The smallest two signals in Panel (b) of Figure 2-4 were collected without a reference beam. We note that even without the reference beam sometimes we could register a large 2Ω signal. Such a large signal can be explained by the interference of a weak modulated signal with a non-modulated component, reflected from sample-probe system (self-homodyning). There is no phase control of such a reflected beam and therefore the signal amplification is random. The signal represented by the dashed line was collected when self-homodyning did not occur; we cannot distinguish signal from the noise in this case.

When we add reference beam to the system, without additional tuning of the apparatus we are able to see strong AC signal. It is possible to see from Figure 2-4 that we strongly amplify our scattered signal as the result of homodyne detection; the absolute value of the amplification depends on the presence of self-homodyning in the absence of the reference field. The control of the absolute value of amplification is illustrated in Panels (a) and (b) of Figure 2-4, while a more qualitiative illustration may be seen in Panels (c) and (d). The upper part of the near field image in Panel (d) shows that without homodyne amplification, the signal is weak and image quality is poor (above arrow), but when the automating homodyning mechanism is activated (below arrow) the signal is stronger and the image quality is much improved. An explanation for the enhanced absorption by the small dots of silicon seen in Panels (c) and (d) is beyond the scope of this thesis.

2.4. Polarizability of the tip-sample system and magnitude of the detected signal

Lock-in detection of the second harmonic signal relies on the strong non-linearity of the detected signal with respect to the probe's position above the sample. In our measurements the amplitude of the cantilever oscillation is comparable to the mean probe-sample distance; therefore we cannot use the perturbation approach to predict the value of the lock-in detected signal. In order to apply an analytical model to explain the detected signal, we have to model the perturbation of the scattered radiation by the oscillating probe explicitly and use the results of such a model to generate a lock-in signal numerically. In our calculations, we considered harmonic motion of the probe above the surface with amplitude A and mean probe-sample distance z_{mean}:

$$z(t) = z_{mean} + A \times \cos(2\pi\Omega t). \tag{6}$$

Here $z(t)$ is the distance (time-dependent) of the probe above the surface and, Ω is the frequency of the cantilever oscillation. For each value of z_{mean}, corresponding amplitude was extracted from the amplitude *vs.* distance dependence, collected simultaneously with the near-field signal. Values of instantaneous probe position were used in a quasi-electrostatic model[27] to calculate the time dependence of the effective polarizability for the oscillating probe-sample system. Because the real part of permittivity of gold at ~1000 cm^{-1} is large, the quasi-electrostatic model for *p*-polarized radiation from Reference 27 can be simplified to:

$$\alpha_{eff} = \frac{8\pi a^3}{1 - \frac{a^3}{4(a+z)^3}}, \tag{7}$$

where a is the radius of the probe, and z is the probe-sample separation. For each value of the mean probe-sample separation, the modulation in the polarizability due to probe's oscillation

was calculated. The intensity of the scattered radiation is proportional to the square of the polarizability.[28] Therefore the homodyne-detected signal is proportional to the absolute value of polarizability. Lock-in detection of the second harmonic signal was modeled by a calculation of the numeric sine and cosine transforms of the polarizability *vs.* time dependence at the twice the frequency of the oscillating cantilever.

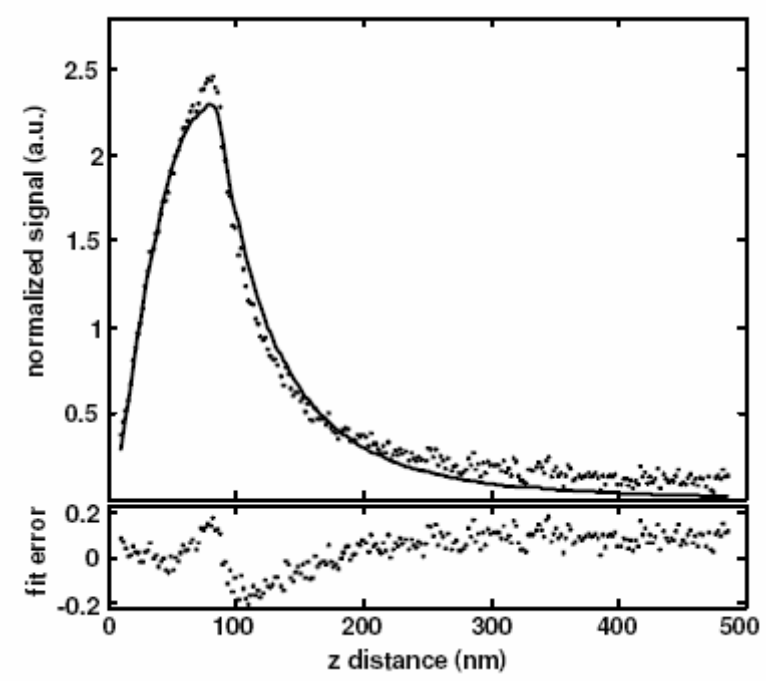

Figure 2-5 Top panel shows the fit of the one scattering sphere model for the near-field signal. In the model, the sphere oscillates above the surface. The bottom panel shows the fit error.

Our calculations indicate that such a model does not simultaneously explain the presence of the long-distance tail (z > 100 nm) in the data, as shown in Figure 2-5. This can be expected since our probe is not a nanometer-sized sphere but extends significantly further away from the surface. A second spherical scatterer, placed right above the first scatterer was included in the

model in order to describe the shape of the probe more realistically (see insert in Figure 2-6). The near-field signal was calculated as a weighted sum of two terms, calculated according to Equation 6 with different radii *a*. The fit parameters were these radii and the weight factors used in adding two terms. The model uses the same values of the radii for different experimental sets, the resulting values are 120 nm and 900 nm. Figure 2-6 shows the normalized data (points) and calculated dependence (solid lines) for three data sets with different level of reference beam intensity and one data set collected without the reference. The ratio of the scaling factors for two scatterers was 90 ±10, which can be explained by the enhancement of the electrical field near the sharp end of the probe (lightning rod effect[29]).

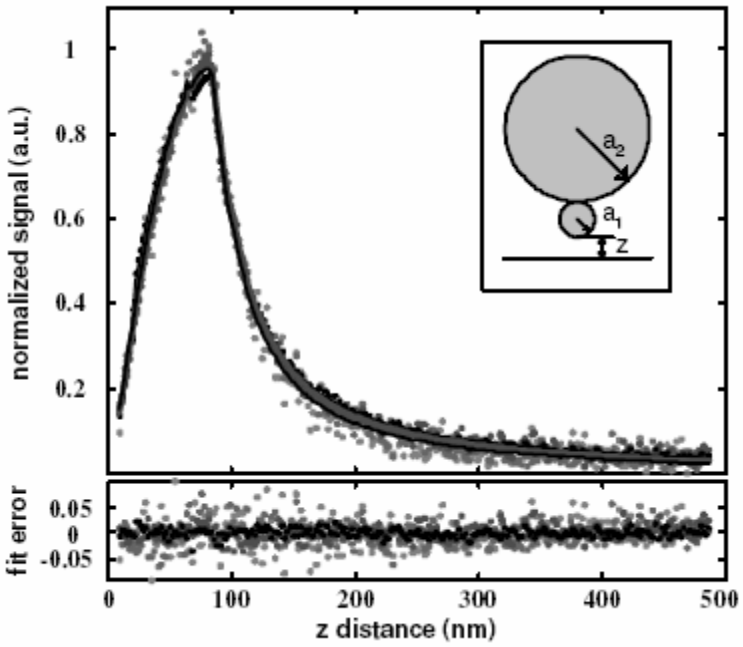

Figure 2-6 The top panel shows the normalized near-field signal-distance dependence (dots) and curves calculated according to the model described in the text (solid lines). The bottom panel shows the fit error.

The nearly perfect overlap of the curves in Figure 2-6 indicates that the data collected without a reference beam were self-homodyned; light reflected back from the cantilever-sample system acted as a reference beam in this case. This explains why it is often difficult to tune an apparatus without the reference beam: overlap between relatively high intensity reflected radiation and the light scattered from the probe is required at the detector. With a reference beam there is a convenient means to control the back-reflected radiation. We note that Knoll and Keilmann[27] have previously reported the benefits of homodyne amplification in apertureless IR near-field scanning microscopy, where a lens was used to simultaneously adjust the focus and phase of a self-homodyning field. We believe our design brings the advantage of independent control of focus and phase in a reference field.

The noise calculated for the smallest AC signal, represented by dashed line in Panel (b) of Figure 2-4 is 0.034 a.u. The standard deviations from the fit to the described above model for the other four signals are in the range from 0.031 to 0.037 a.u. Thus, we can say that we fit distance dependencies well and the fit errors represent the noise level in the AC signals. Since the noise is almost the same for all signals in Figure 2-4, and the signal without interferometric amplification is about 1:1, we conclude that signal-to-noise ratio is improved by as much as 150 times by utilizing interferometric amplification.

BIBLIOGRAPHY

1. J. Wessel, J. Opt. Soc. Am. B. **2**, 1538 (1985).
2. Nemetz, and A. Knoll, J. Raman Spectrosc. **27**, 587 (1996).
3. Piednoir, C. Licoppe, and F. Creuzet, Opt. Comm. **129**, 414 (1996).
4. Cricenti, Appl. Surf. Sci. **162**, 275 (2000).
5. Lahrech, R. Bachelot, P. Gleyzes, and A. C. Boccara, Opt. Lett. **21**, 1315 (1996).
6. Y. Inouye and S. Kawata, Opt. Lett. **19**, 159 (1994).
7. Michaels, S. J. Stranick, L. J. Richter, and R. R. Cavanagh, J. Appl. Phys. **88**, 4832 (2000).
8. Dragnea and S. R. Leone Int. Rev. Phys. Chem. **20**, 59 (2001).
9. Knoll and F. Keilmann, Nature **399**, 134 (1999).
10. F. Zenhausern, Y. Martin, and H. K. Wickramasinghe, Science, **269** 1083 (1995).
11. M. Adams, J. Kerimo, C. Y. Liu, A. J. Bard, and P.F. Barbara, J. Phys. Chem. B **104**, 6728 (2000).
12. O. Cherniavskaya, S. Kaemmer, S. Schiering, J. Coffin, and D. M. Adams, submitted.
13. V. Deckert, D. Zeisel, R. Zenobi, and T. Vo-Dinh, Anal. Chem. **70**, 2646 (1998).
14. Higgins, X. Liao, J. Hall, and E. Mei, J. Phys. Chem. B **105**, 5874 (2001).
15. E.-S. Kwak, T. J. Kang, and D. A. Vanden Bout, Anal. Chem. **73**, 3257 (2001).
16. H. F. Hamann, A. Gallagher, and D. J. Nesbitt, App. Phys. Lett. **73**, 1469 (1998).
17. R. D. Schaller, J. C. Johnson, K. R. Wilson, L. F. Lee, L. H. Haber, and R. J. Saykally, J. Phys. Chem. B **106**, 5143 (2002).
18. G. M. H. Knippels, T. I. Smith, H. A. Schwettman, and D. V. Palanker, Optics Comm. **148,** 215 (1998).
19. Zumbusch, G. R. Holtom, and X. S. Xie, Phys. Rev. Lett. **82**, 4142 (1999).

20. B. Akhremitchev, S. Pollack, and G. C. Walker, Langmuir, **17**, 2774 (2001); B. B. Akhremitchev and G. C. Walker, Bull. Chem. Soc. Jpn. **75**, 1011 (2002).

21. P. M. Bridger and T. C. McGill, *Opt. Lett.* **24**, 1005 (1999).

22. R. Hillebrand and F. Keilmann, *Phys. Rev. Lett.* **85**, 3029 (2000).

23. J. Azoulay, A. Debarre, A. Richard, and P. Tchenio, *Appl. Opt.* **39**, 129 (2000).

24. Y. Sasaki and H. Sasaki, *Jpn. J. Appl. Phys.* **39**, L321 (2000).

25. B. Akhremitchev, Y. Sun, L. Stebounova, and G. C. Walker, Langmuir **18,** 5325 (2002).

26. N. Maghelli, M. Labardi, S. Patane, F. Irrera, and M. Allegrini, J. Microscopy **202**, 84 (2001).

27. Knoll and F. Keilmann, Opt. Commun. **182**, 321 (2000).

28. F. Bohren and D. R. Huffman, *Absorption and scattering of light by small particles* (Wiley & Sons, New York, 1983).

29. Wokaun, Solid State Physics 38, 223 (1984).

3. MONOLAYER-SENSITIVE INFRARED IMAGING OF DNA STRIPES USING APERTULESS NEAR-FIELD MICROSCOPY[§]

Monolayer-sensitive chemical imaging with a lateral spatial resolution of approximately 200 nm is demonstrated. Apertureless near-field scanning infrared microscopy was employed to study samples patterned with regions of DNA and hexadecanethiol. The scattering of the infrared radiation was modulated by an oscillating metallic probe, and the scattered signal was demodulated at twice the probe's oscillation frequency. The maps of the near-field signal reveal patterns that are not readily observable in the topographic images, indicating the absence of topography-related artifacts. The decrease in the scattering from areas coated with 24 base-pair long DNA molecules is attributed to a phosphate stretching absorption band. The near-field absorption is observed to be larger than the far-field absorption.

3.1. Introduction

Recent progress in near-field microscopy is stimulating a continuously growing interest in chemical imaging on the nanometer scale.[1-9] The apertureless type (sometimes called the scattering type) of near-field microscopy provides unsurpassed resolution for imaging over broad regions of the electromagnetic spectrum. [10-13] Vibrational sensitivity with 10^{-8} - 10^{-7} m spatial

[§] This work has been published as (except for Figure 3-4) B. Akhremitchev, Y. Sun, L. Stebounova, and G. C. Walker, *Langmuir* **18,** 5325 (2002), and Figure 3-4 was published in Akhremitchev, B. B.; Bemis, J. E.; Al-Maawali, S.; Sun, Y.; Stebounova, L.; Walker, G. C., *Biofouling* **19** Suppl, 99 (2003).

resolution is achieved either *via* strong enhancement of the Raman signal that is enabled by using nanometer-sized antennae and electronic absorption of the sample[4] or by detecting the attenuation of scattered infrared radiation.[1,6,10,14] While Raman near-field microscopy provides high resolution and the possibility to measure the entire vibrational spectra of the molecules, its use is typically limited by very small non-resonant Raman cross-sections and therefore the necessity to rely on electronic resonance enhancement of the cross-section. By using infrared (IR) absorption it is possible to study samples without depending on electronic absorption, and this is particularly useful for studies of polymers and biomolecules. A prominent challenge has been to reduce the minimum detected number of absorbing chromophores. In this paper we report what we believe to be the first use of a near-field scanning infrared microscopy to study the infrared absorption of a molecular monolayer, in this case a sub-monolayer of DNA.

3.2. Experimental details

We use a home-built apparatus that is based on a commercial atomic force microscope (MultiMode AFM, Digital Instruments Inc., Santa Barbara, CA). The optical scheme of the instrument is shown in Figure 3-1. The IR radiation from tunable carbon dioxide laser is directed toward a reflecting IR objective by a ZnSe partial (50/50) reflector (II-VI Inc., Saxonburg, PA). Radiation is focussed by an IR objective (0.28 NA, Coherent Inc., Auburn, CA) onto the end of a platinum-coated cantilever probe, perpendicular to the long axis of the probe. We use *p*-polarized light with an ~80° angle of incidence. The spot size is approximately 50 μm, and the laser radiation power is 20-100 mW.

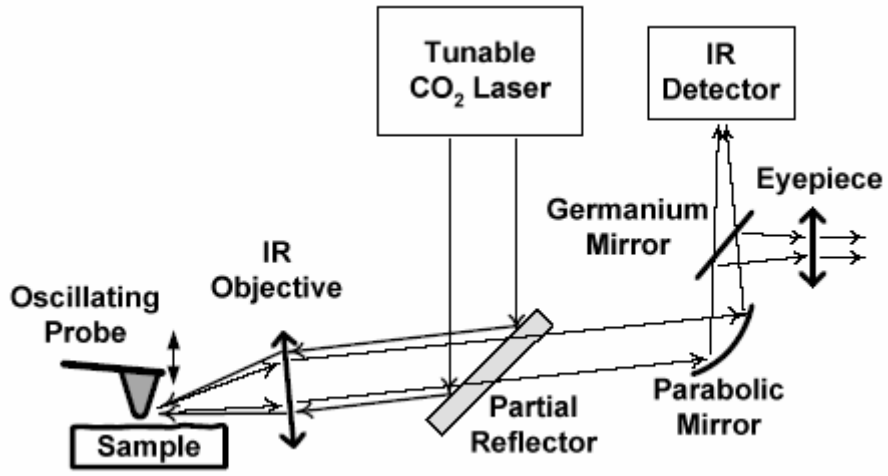

Figure 3-1 Schematic of the apertureless near-field infrared microscope.

The probe is a commercial silicon probe (MikroMasch, Tallinn, Estonia) coated with 25 nm of platinum. To assist the focussing of the invisible CO_2 laser radiation, we co-propagate the IR beam with the visible radiation from a He-Ne laser prior to partial reflector (the He-Ne laser is not shown in Figure 3-1). The IR radiation scattered by the probe and the sample propagates back through the same IR objective and the partial reflector. We use a paraboloidal mirror (effective focal length 127 mm, Janos Technology Inc., Townshend, VT) to focus the back-scattered radiation onto a MCT infrared detector (Graseby Infrared, Orlando, FL). A germanium mirror in the path of the infrared radiation reflects the visible radiation, aiding in the visual inspection of the probe. All of the optical components described above, except the IR detector and the lasers, are rigidly attached on a platform, which is mounted atop an XYZ translational stage. The IR detector is mounted on a separate translational stage to enable adjustment of the position of the focussed radiation on the sensing element. This design facilitates the tuning of the focussed IR beam onto the end of the cantilever and the direction of collected radiation onto

the detector. The electrical signal from the IR detector's preamplifier is further amplified by a lock-in amplifier (SR844, Stanford Research Systems Inc., Sunnyvale, CA) and collected by a computer, simultaneously with the AFM data. We used either the cantilever oscillation signal or the harmonic of this signal as reference signals in lock-in detection.

The far-field absorption spectra of DNA grafted onto gold substrates were collected with an FTIR spectrometer (Thermo Nicolet, Madison, WI) equipped with a specular reflection accessory (Model 500, Spectra-Tech, Shelton, CT) tuned for a 75^{o} angle of incidence. Bare, ungrafted gold-coated substrates were used to collect the reference spectra.

The patterned DNA samples were prepared as follows. Glass substrates were coated with gold (100 nm) by vacuum evaporation. Micro-contact printing[15] was employed to create stripes of 1-hexadecanethiol. The presence of ~5 μm wide stripes of 1-hexadecanethiol was confirmed by AFM topography imaging. Patterned gold substrates were incubated in a thiolated DNA solution (0.25 mM solution of 24-Cytosine single strand 3'-tholated DNA oligomer in deionized water). After incubation, the substrates were cleaned of excess DNA by sonication in deionized water and dried in a stream of nitrogen gas. All samples were used within two days of preparation.

3.3. Distance dependence of the near-field signal

Modulation of the scattered radiation by oscillating a probe near the sample's surface is one of the most common features of detection of a near-field signal. Lock-in detection at the frequency of probe oscillation (*f*) is often used in order to filter the near-field signal from the large background. It has been noted that the distance dependence of such a signal is often non-monotonic, which has been attributed to the interference of radiation from different sources.[1] In

other words, the signal detected at frequency *f* might have a significant component that is not specific to the surface just under the tip. Due to the large spot size of the focused IR beam, a significant portion of the cantilever is illuminated, providing a background contribution to the detected scattered signal. The scattered signal that is detected at the cantilever oscillation frequency might have a significant component due to this background scattering. Detection of the scattered signal at the twice the frequency of the probe's oscillation provides a convenient way to extract the surface-specific signal.[16,7,17] It has been established that probe oscillation upon approach toward the surface remains harmonic (see, for example, reference 18), thus the presence of the second harmonic in the scattered signal indicates strong non-linearity in the near-field signal upon approach to the surface. A coupled-dipoles model[19] predicts a non-linear polarizability modulation of the spherical tip and sample of radius *a* upon tip-sample separation *r*:

$$\Delta\alpha \propto \frac{1}{\left(a^2 + r^2\right)^{\frac{3}{2}}}.$$

Figure 3-2 shows both the distance dependence of the cantilever oscillation amplitude (top panel) and the scattered IR signals, lower panel. For brevity, we will call the signals that are collected at one and two times the frequency of the cantilever oscillation the *f*- and *2f*-signals, respectively. The *2f*-signal amplitude in Figure 3-2 has been multiplied by 10 for it to appear on the same graph as the *f*-signal. It can be noted that in the region where the cantilever oscillation amplitude is relatively constant (30-200 nm from the surface), the *2f*-signal decreases monotonically with increasing tip-surface separation, while the *f*-signal does not. Non-monotonic dependencies can produce artifacts during imaging. At distances less than ~30 nm the amplitudes of both signal decay because of mechanical damping of the probe oscillation by the surface.

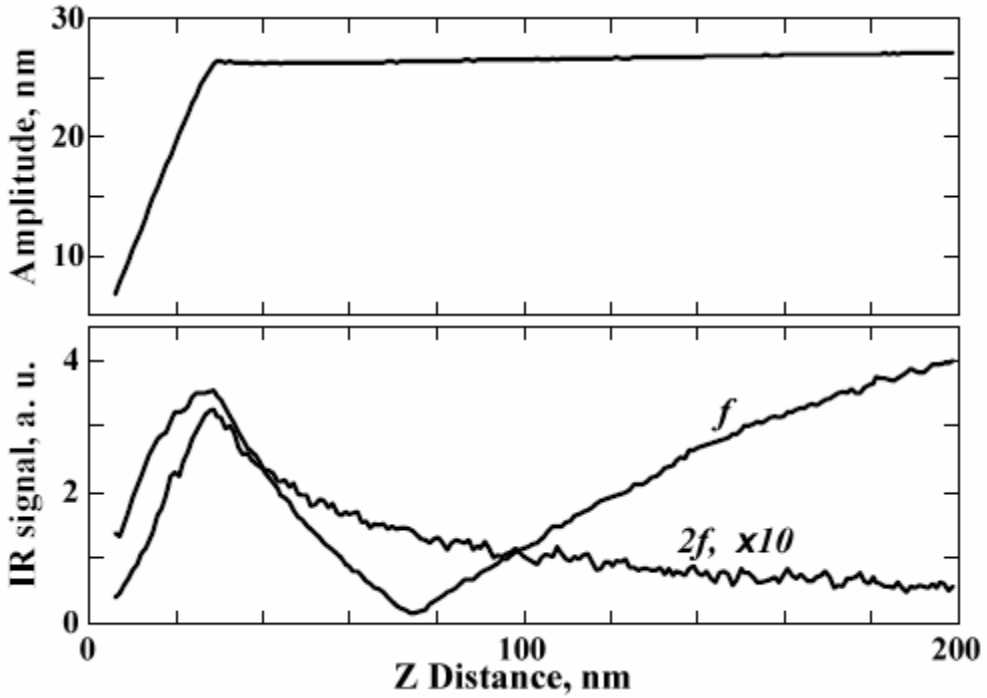

Figure 3-2 The top panel shows how the amplitude of the vertical probe oscillation depends on the separation from the surface. The bottom panel shows IR signals demodulated at the frequency of the probe oscillation (f) and twice the oscillation frequency (2f). The interferometric feature present in the f-signal is missing from the 2f-signal.

3.4. Submonolayer chemical sensitivity of the near-field apparatus

We have performed simultaneous topography and *2f*-signal mapping of a surface patterned with alternating DNA and 1-hexadecanethiol stripes. Figure 3-3 shows two 20 μm x 20 μm images collected with a ~ 100 nm peak-to-peak amplitude of tip oscillation at ~133 kHz. The near-field signal was acquired using 980 cm^{-1} radiation, which corresponds to the phosphate IR absorption band of DNA.[20] Lock-in detection at *2f* (~266 kHz) was accomplished with a 3 ms time

constant. The scan rate was 0.3 Hz. The mean near-field *2f*-signal collected during scanning corresponds to ~0.5 nW of IR radiation power incident on the detector, modulated at *2f*. The striped pattern from the contact printed surface is visible in the topography image, although sharp edges of the DNA stripes are not readily discernable in this image.

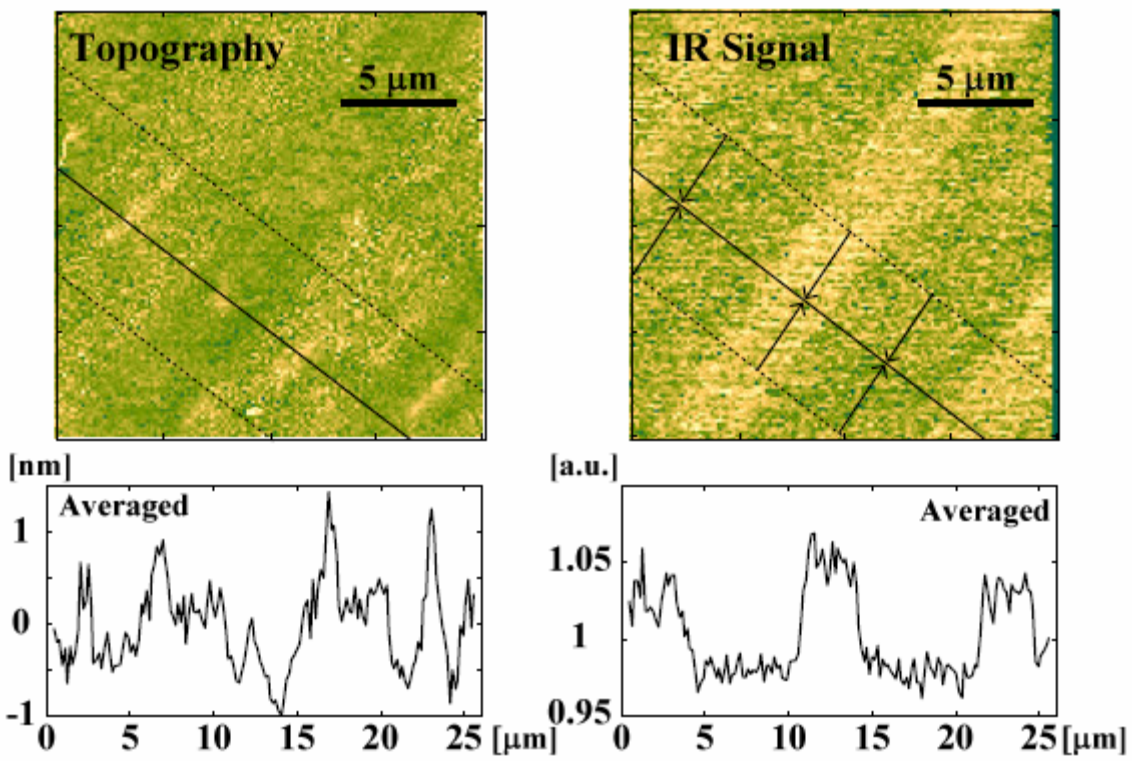

Figure 3-3 The image on the left shows the topography of the striped DNA- hexadecanethiol sample; the image on the right shows the *2f* infrared signal. The 10 μm stripe pattern can be easily seen in the IR signal image; DNA regions are darker than alkanethiol regions. Several height features that are discernable in the topographic image are not coupled to IR signal. Graphs below each image show the projection of the signal from a 7.5 μm wide area onto a line perpendicular to the linear pattern, as indicated in the corresponding images.

The near-field image shows a periodic variation corresponding to the periodicity and structure of the stamp that was used in the sample's preparation. From the images we see that the near-field map does not directly correlate with the topographic map; the cross-correlation coefficient between images is –0.15. Tip motion coupling into the near-field signal, also known as *z*-motion artifact, [21] is usually responsible for topographic artifacts in the constant gap scanning method that was employed here. Because there is a low correlation between the topography and the near-field signal in Figure 3-3, we conclude that the near-field signal is not topography-coupled. In order to compare signals in the regions covered with hexadecanethiol and DNA, we project signals from 7.5 μm wide areas, as indicated with dashed lines in the images, onto a line perpendicular to the direction of the linear pattern. Averaged topography and *2f*-signal graphs are shown below the corresponding images. These graphs convincingly demonstrate the absence of coupling between the near-field signal and the topography. We note that not all images of the patterned DNA sample that we have collected have such a low correlation between topography and *2f*-signal as the images in Figure 3-3. The highest degree of coupling corresponds to cross-correlation between maps of approximately –0.5 (data not shown). Images with better-defined topography compared to that shown in Figure 3-3 indicate that the DNA layer is ~2 nm thicker than hexadecanethiol layer. The small thickness of the DNA monolayer indicates that the DNA molecules are not closely packed on the surface and that the molecules extend from the surface by approximately half of their backbone length.

A line plot of the IR signal in Figure 3-3 shows that the *2f*-signal from the DNA monolayer is ~7% weaker than the signal from the hexadecanethiol monolayer. This Figure shows remarkably strong IR contrast for just one monolayer of molecules, though magnitude of this difference varies significantly from image to image collected under similar conditions. In order to obtain a

mean value of the IR contrast, we have averaged images together at different wavelengths of IR radiation in the phosphate backbone IR absorption region. Distinct topographic features were used to align the images during averaging. Figure 3-4 shows the IR contrast signal resulting from averaging the *2f*-signal at different wavelengths and the far-field IR absorption spectrum of DNA monolayer. We note a very broad and featureless far-field absorption band, characteristic of surface absorbed DNA;[22] the broad width of the phosphate band precluded measurement across the entire band because of the limited tunability of CO_2 laser. The averaging process used here reduces the microscopes sensitivity to small length-scale chemical heterogeneity.

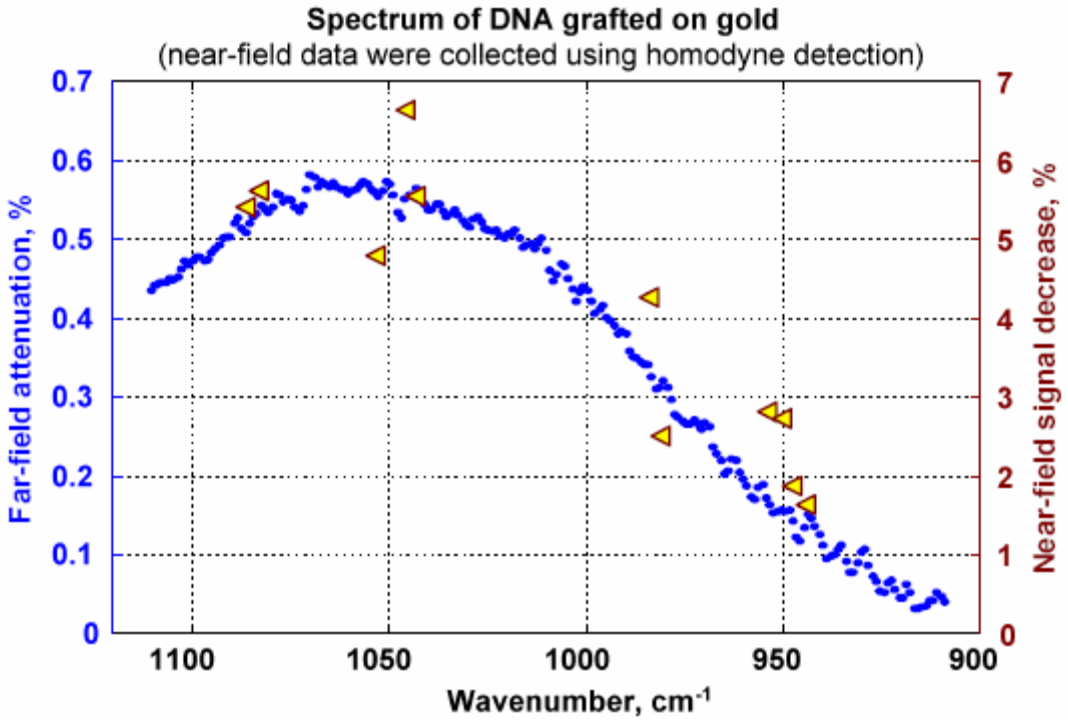

Figure 3-4 The graph shows the far-field IR absorption of a DNA monolayer grafted onto a gold substrate, in the spectral region of phosphate absorption band (dotted line). The figure also shows the result of averaging the near-field IR images at different wavelengths (triangle symbols).

The near-field absorption follows the same wavelength dependence as the far-field absorption, further confirming that contrast in our near-field images is caused by varying chemical composition. The averaged near-field absorption of DNA (~7%) is bigger than far-field absorption. The enhanced IR absorption in the near-field could be related to the well-known phenomenon of surface-enhanced infrared absorption.[23] In our case the increase of absorption could be explained by an electric field enhancement[24,25] under the metallic tip. Alterations in the IR absorption strength could be due to tip shape modification or tip contamination during imaging.

We have estimated the resolution of monolayer-sensitive near-field IR imaging by examining the sharpness of the edge of the DNA absorption features; the resolution corresponds to approximately 200 nm (10-90% transition). It is likely that this resolution is worse than the limit attainable with our microscope, and that with a higher signal-to-noise ratio the resolution could be approaching the size of the probe of ~50 nm. The resolution achievable in apertureless near-field infrared microscopy is ~15-30 nm, and is limited by a combination of factors, such as the size of the probe and the scan height above the surface.[12,14] Also, an estimate of resolution using the edge width depends on actual sharpness of the features. We think that these factors explain why our estimated resolution is not as good as that obtained by others. An area with a diameter of 200 nm for ~3 nm thick DNA monolayer corresponds to a signal from $\sim 5 \cdot 10^5$ phosphate groups ($\sim 10^{-18}$ moles). It is possible that the number of absorbing phosphate groups is much less due to DNA chain orientation, and that our actual sensitivity is even higher.

3.5. Conclusions

We have demonstrated monolayer sensitivity in near-field scanning infrared microscopy by detecting contrast from a DNA/alkane patterned sample. Chemical contrast imaging was achieved by examining IR absorption in the spectral region of the phosphate stretching band of DNA molecules and harmonic demodulation of the signal scattered by the oscillating probe. IR absorption maps revealed that the IR signal was not coupled to the vertical tip motion, indicating artifact-free imaging. We have observed a strong IR absorption from the regions grafted with DNA, and we speculate that the enhancement of the infrared absorption in our experiments has the same origin as the phenomenon of surface-enhanced infrared absorption. The observed contrast corresponds to detection of $\sim 10^{-18}$ moles of phosphate groups, with ~200 nm lateral resolution. Technological advances in detecting the weak IR signal will provide even higher resolution and sensitivity.

BIBLIOGRAPHY

1. Akhremitchev, B. B.; Pollack, S.; Walker, G. C. *Langmuir* **2001**, *17*, 2774-2781.

2. Dragnea, B.; Leone, S. R. *International Reviews In Physical Chemistry* **2001**, *20* (1), 59-92.

3. Michaels, C. A.; Stranick, S. J.; Richter, L. J.; Cavanagh, R. R. *J. Appl. Phys.* **2000**, *88*, 4832-4839. Barbara, P. F.; Adams, D. M.; O'Connor, D. B. *Annual Review of Materials Science*, **1999,** *29*, 433-469.

4. Stockle, R. M.; Suh, Y. D.; Deckert, V.; Zenobi, R. *Chem. Phys. Lett.* **2000**, *318*, 131-136. Hayazawa, N; Inouye, Y.; Sekkat, Z.; Kawata, S. *Chem. Phys. Lett.* **2001**, *335*, 369-374. Nieman, L. T.; Krampert, G. M.; Martinez, R. E. *Rev. Sci. Instrum.* **2001**, *73*, 1691-1699.

5. Azoulay, J.; Debarre, A.; Richard, A.; Tchenio, P. *Appl. Opt.* **2000**, *39*, 129-134.

6. Hillenbrand, R.; Knoll, B.; Keilmann, F. *J. Microscopy* **2001**, *202*, 77-83.

7. Maghelli, N.; Labardi, M.; Patane, S.; Irrera, F.; Allegrini, M. *J. Microscopy* **2001**, *202*, 84-93.

8. Anderson, M. S. *Appl. Phys. Lett.* **2000**, *76*, 3130-3132.

9. Hamann, H. F. *Zeitschrift fur Physikalische Chemie* **2001**, *215*, 1025-1042.

10. Lahrech, A.; Bachelot, R.; Gleyzes, P.; Boccara, A. C. *Appl. Phys. Lett.* **1997**, *71*, 575-577.

11. Zenhausern, F.; O'Boyle, M. P.; Wickramasinghe, H. K. *Appl. Phys. Lett.* **1994**, *65*, 1623-1625.

12. Knoll, B.; Keilmann, F. *J. Microscopy* **1999**, *194*, 512-515.

13. Knoll, B.; Keilmann, F.; Kramer, A.; Guckenberger, R. *Appl. Phys. Lett.* **1997**, *70*, 2667-2669.

14. Gresillon, S.; Ducourtieux, S.; Lahrech, A.; Aigouy, L.; Rivoal, J. C.; Boccara, A. C. *Appl. Surf. Sci.* **2000**, *164*, 118–123.

15. Xia, Y.; Whitesides, G. M. *Annu. Rev. Mater. Sci.* **1998,** *28*, 153–184.

16. Wurtz, G.; Bachelot, R.; Royer, P. *Eur. Phys. J. Appl. Phys.* **1999**, *5*, 269-275.

17. Knoll, B.; Keilmann, F. *Opt. Commun.* **2000**, *182*, 321-328.

18. Anczykowski, B.; Gotsmann, B.; Fuchs, H.; Cleveland, J. P.; Elings, V. B. *Appl. Surf. Sci.* **1999**, *140*, 376-382.

19. Zenhausern, F.; Martin, Y.; Wickramasinghe, H. K. *Science* **1995**, *269*, 1083-1085.

20. Taillandier, E.; Liquier, J. *Methods Enzymol.* **1992**, *211*, 307-335.

21. Hecht, B.; Bielefeldt, H.; Inouye, Y.; Pohl, D. W.; Novotny, L. *J. Appl. Phys.* **1997**, *81*, 2492-2498.

22. Boncheva, M.; Scheibler, L.; Lincoln, P.; Vogel, H.; Akerman, B. *Langmuir* **1999,** *15,* 4317-4320.

23. Osawa, M. *Top. Appl. Phys.* **2001**, *81*, 163-187.

24. Martin, O. J. F.; Girard, C. *Appl. Phys. Lett.* **1997**, *70*, 705-707.

25. Larsen, R. E.; Metiu, H. *J. Chem. Phys.* **2001**, *114*, 6851-6860.

4. FIELD ENHANCEMENT IN VERY SMALL APERTURE LASERS STUDIED BY APERTURELESS NEAR-FIELD MICROSCOPY

Localized surface plasmons have been observed on very small aperture lasers using apetureless near-field microscopy. The near-field optical pattern around the aperture indicates the interference of surface plasmons with incident light. A surface plasmon point-source model has been used to determine the wavelength and the decay length of surface plasmons at the Al/Si_3N_4 interface. Near-field measurements also confirmed a preferred orientation of the rectangular aperture waveguide for the signal enhancement in very small aperture lasers.

4.1. Introduction

The evanescent nature of surface plasmons has attracted many researchers in the past decade for their applications in devices requiring localized fields and for chemical sensing. Surface plasmons (SPs) are non-radiative modes of electromagnetic fields present at metal/dielectric interfaces.[1] SPs can be excited by coupling of incident photon energy into surface electron vibrations in a total internal reflection geometry used in the Kretschmann configuration.[2] Subwavelength defects made in the metal films have been shown to act as the sources of SPs that are localized due to the dimensions of such fine structures when the metal/dielectric interface is illuminated under normal incidence of light.[3-5] Exciation of surface plasmons at the

dielectric/metal interface has also found its applications in surface-enhanced absorption spectroscopy[6] and Raman spectroscopy.[7]

Recently, SPs have been used to enhance the emission of light from light emitting diodes covered with thin metal films.[8,9] New mechanisms of SPs excitation applicable to such devices have been discussed.[8] This mechanism involves the energy transfer between semiconductor quantum wells (QWs) and metal/dielectric surface plasmons.[9] Electron-hole pairs excited in the QWs couple to the surface electron vibrations when their energies are similar. Subwavelength apertures fabricated on a semiconductor laser covered with a thin layer of metal affect the mechanism of coupling light out of a diode.[10] In this letter we provide experimental evidence that the excitation of surface waves is coupled to the resonant transmission of a metal slit[11] positioned over a laser diode.

4.2. Experimental details

We have used near-field scanning optical microscopy (NSOM) to analyze the generation and localization of surface plasmons in a submicron aperture at the dielectric/metal interface of very small aperture lasers (VSALs). VSALs promise to be efficient light sources for near-field optical recording.[10, 12, 13] In such devices the light is emitted through an aperture that was etched in the metal layer to expose the active region beneath the metal.[14] The evanescent field present on the dielectric/metal interface of a very small aperture laser has been reradiated using an apertureless near-field probe.[15] In our setup a platinum-coated silicon tip (MikroMasch, Tallinn, Estonia) is oscillated in close proximity the the aperture, perpendicular to the metal surface. The oscillation occurs near the cantilever's resonant frequency, which is about 150kHz. Lock-in detection of the

modulated scattered signal at the frequency of cantilever oscillation is performed using the integrated photodetectors available on the laser package. Figure 4-1 shows the position of integrated detectors on the laser diode and the geometry of near-field setup.

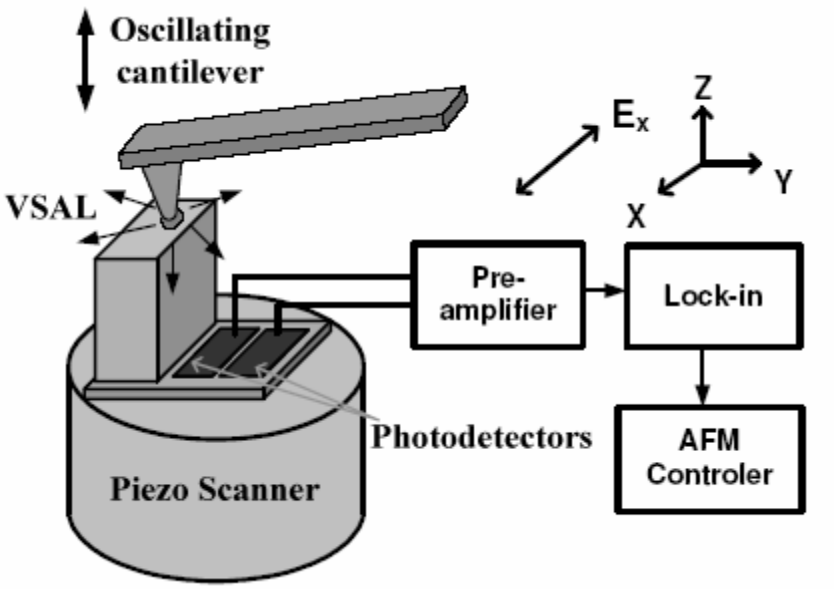

Figure 4-1 Geometric relations of the apertureless NSOM components for the imaging of VSAL.

4.3. Dispersion of aluminum surface plasmons

Semiconductor lasers used in the experiment have an index-guided, multiple quantum well structure. Their quantum wells consist of GaInP layers with an energy gap of 1.9 eV, separated by layers of AlGaInP. The aluminum coating deposited on top of the laser diode is 50 nm thick,

and it is separated from quantum wells by a 50 nm Si_3N_4 spacer. The energy of surface plasmons at the Al/Si_3N_4 interface is lowered by the dielectric constant of Si_3N_4:

$$\hbar\omega_{sp} = \frac{\hbar\omega_p}{(1+\varepsilon_{SiN})^{1/2}}, \tag{8}$$

where $\hbar\omega_p$ = 15 eV is the excitation energy of volume plasmons in Al,[16] and ε_{SiN} = 4.2 is the dielectric constant of Si_3N_4.[17] By substituting these numbers into Equation (8) we obtain $\hbar\omega_{sp}$ = 6.4 eV.

Although the energy match between the optical field and SPs in Al film is not ideal, it has been shown that Al is suitable for SP excitation in the visible region.[9] The dispersion curve for Al surface plasmons can be calculated from the following dispersion relation:[18]

$$k_{sp} = k_{inc}\sqrt{\frac{\mathrm{Re}(\varepsilon_{Al})*\varepsilon_{SiN}}{\mathrm{Re}(\varepsilon_{Al})+\varepsilon_{SiN}}},$$

where Re(ε_{Al}) is frequency dependent real part of dielectric constant for Al obtained from ref. 17, and $k_{inc}=2\pi/\lambda_{inc}$ is wave vector of the incident photons. Figure 4-2 shows the dispersion diagram for SPs on Al/Si_3N_4 interface.

The wavelength of surface plasmons can be found using the following equation:

$$\lambda_{sp} = \lambda_{inc}\left(\frac{\mathrm{Re}(\varepsilon_{Al})+\varepsilon_{SiN}}{\mathrm{Re}(\varepsilon_{Al})*\varepsilon_{SiN}}\right)^{1/2},$$

λ_{inc} is the wavelength of the incident photons. By substituting Re(ε_{Al}) = -58.95 at λ_{inc} = 655 nm into this equation we obtain λ_{sp} = 308 nm.

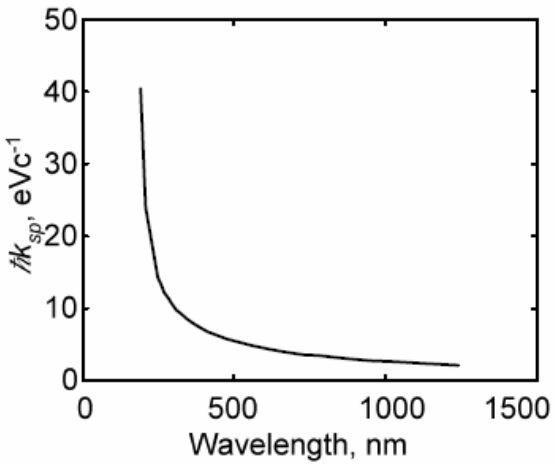

Figure 4-2 Dispersion diagram of surface plasmons generated at Al/Si_3N_4 surface.

4.4. Interference of surface plasmons with an optical field

We have imaged a near-field optical pattern around the nanoaperture, which was made using a focused ion beam etcher (FIB) in Al film on top of laser diode.[14] Figure 4-3a shows an AFM topography image of the aperture. The dimensions of the aperture are 400 nm x 100 nm. Other topographic features seen in this image correspond to defects in Al film and were present in the FIB image (not shown) after the etching of the aperture. The height of the biggest feature in the topography image was no more than 50 nm. The image scan size was 1500 nm x 1500 nm. Figure 4-3b and c show near-field signals near the aperture collected using the integrated photodetectors situated on a side of laser diode in y direction below the aperture (see Figure 4-1 for the detector's position). The x-polarized light propagated in the z direction, from the back to the front. The laser diode was rotated 90 degrees in order to collect Figure 4-3c. Note, that the

detectors were rotated with the diode, but the position of the AFM tip remained the same. The near-field signal distribution in these images suggests that we see localized surface plasmons.[19]

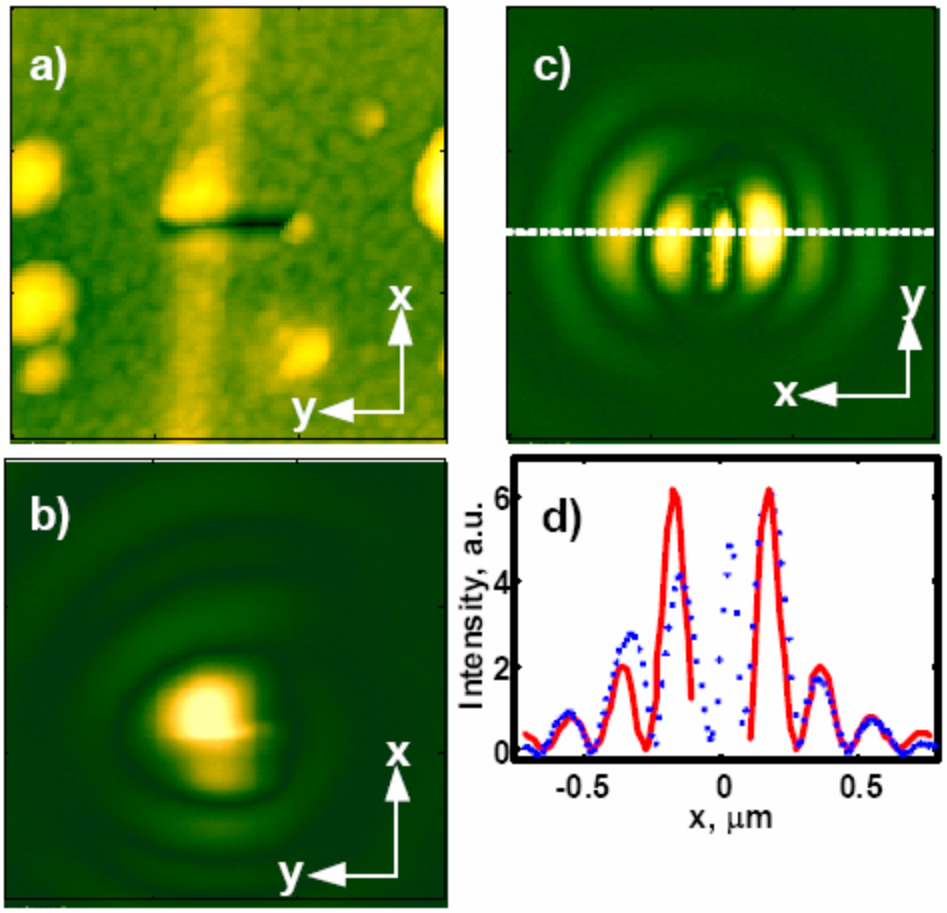

Figure 4-3 (a) Topographic image of the aperture and its surrounding. The dimensions of the aperture were 400 nm x 100 nm. (b), (c) Near-field signals in and near the aperture. The aperture was rotated 90 degrees prior to collecting image (c). The scan area of the images was 1500 nm x 1500 nm. Plot (d) presents a cross section (dotted line) made in image (c) and a fit (solid line) made according to the surface plasmon point-source model.

Without the aperture SPs produce a uniform electric field on the metallic surface.[20] It has been shown that isolated nanoscale holes can act as point-like sources of surface plasmons.[3] The

signals around the aperture in Figure 4-3b and c indicate interference patterns. In our case the aperture made in Al coating goes all the way through the metal film exposing the active layer beneath the coating, so that surface plasmons localized at the aperture may interfere with the incident light. The distances between the fringes in images b and c are about 200 nm.

We used a SP point-source model[3] to fit a line section made along the dashed line in Figure 4-3c. If we assume that the metal film is in *x*-*y* plane, then along *x* and near $z = 0$ the x-polarized field has the following component:

$$E_x = A\exp\left(-\frac{|x|}{d}\right) * \exp\left(ik_{sp}x\right)/|x|^{1/2} + B\,,$$

where A is the amplitude of the decaying field, B is the amplitude of the transmitted light, k_{sp} is the wavevector of surface plasmons, and d is the decay constant. The interference between optical field and surface plasmons can be found as $|E_x|^2$.

Figure 4-3d shows the experimental trace (dotted line) and fit to the model discussed above (solid line). The signal inside of the aperture was not fitted because in this model we do not consider the waveguide modes contributing to near-field signal.[10] The signal on the right side of the aperture has a poor fit probably due to the asymmetry of the scattering of the light by the tip. The fringe's period is expected to be different when the angle of the incidence of the light is not zero.[3] We do not know the exact geometry of the light propagation through the aperture; however, the phase shift of signals on the two sides of the aperture is small, hence we conclude that the incident light is nearly at normal incidence. From our fitting parameters we found the wavelength of surface plasmons, λ_{sp}(fit) = 360nm, which is ~ 15% bigger than the calculated value, and the decay length of SPs, d = 690nm. Since there are no other field patterns associated with the defects on the Al surface, this indicates that the source of the near-field signal comes

from the aperture. Differences between Figure 4-3b and c were examined by rotating the sample to change the direction of scanning the aperture with the tip. The image was collected from the top to the bottom. During the collection of the Figure 4-3b the tip scanned the aperture along its wider side and we observed a wide near-field spot in the aperture. When the tip was scanned in the aperture along its narrow side in Figure 4-3c, we observed a more confined near-field spot in the aperture and stronger interference fringes on the sides in the direction of the field polarization.

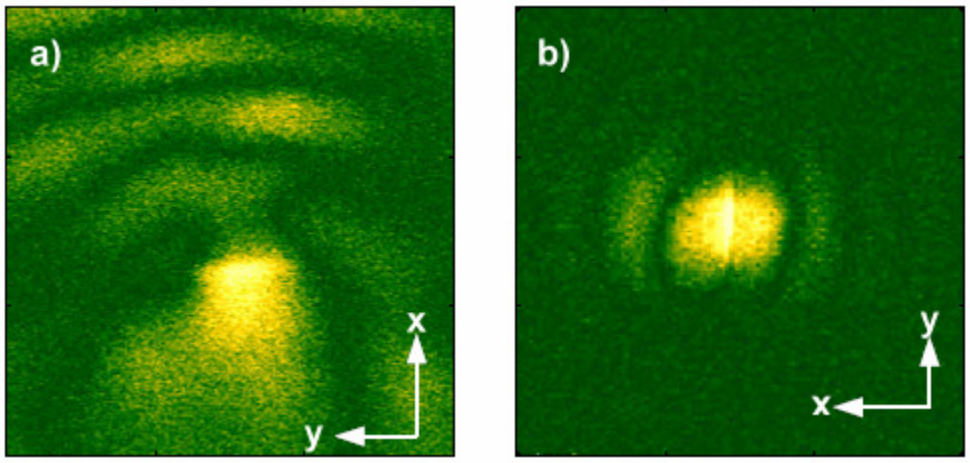

Figure 4-4 Near-field signals collected in and near the aperture shown in Figure 4-3 using external detector. The aperture was rotated 90 degrees prior to collecting image (b). The external detector was not rotated with the aperture.

A similar pattern for two sample rotation angles was obtained using an external detector (Figure 4-4). The description of the near-field system with an external detector has been presented earlier in Chapters 2 and 3. In this experiment the detector remained in the same position and was not rotated with the diode. This confirms that the field is bound to the metal surface and does not

change with the position of the detector. The signal-to-noise ratio has been worse for this detector, and we did not observe many fringes around the aperture, while the confinement of the light in the aperture is very clear in both cases.

4.5. Influence of the aperture orientation on a field enhancement in optical waveguide

We have observed different near-field pattern when three apertures were etched in the Al film on another laser diode.

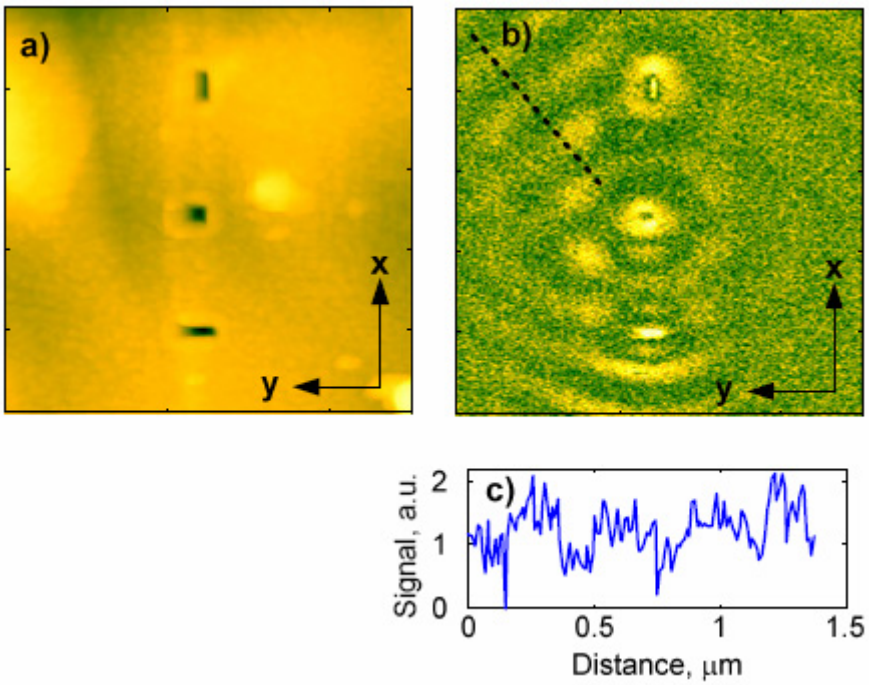

Figure 4-5 (a) Topographic image of three apertures made on Al coated laser diode. (b) Near-field signal collected in the vicinity of the apertures using integrated photodetectors. Image scan area is 2500 nm x 2500 nm. (c) Section line indicated in (b) by dashed line.

Figure 4-5a shows the AFM topography image of the sample. The size of two rectangular apertures was 200 nm x 100 nm, and the size of a square aperture was 140 nm x 140 nm. The image scan size was 2500 nm x 2500 nm. Figure 4-5b is the image of near-field signal collected on this diode using integrated photodetectors. Here again, *x*-polarized electric field propagates in *z* direction. The plot in Figure 4-5c shows the experimental trace along the dashed line indicated in Figure 4-5b. The period of fringes in this image is about 330 nm, or $\lambda_{inc}/2$, which corresponds to an interference between the directly transmitted waves from different apertures. Stronger enhancement of the light is observed in the rectangular aperture which has its longer side perpendicular to the direction of the electric field polarization. The near-field intensity ratio for two rectangular apertures in Figure 4-5b equals to 2.5. The observed difference in the signals for two rectangular apertures in Figure 4-5b coincides with the far-field measurements and waveguide theory predictions for the aperture shape effect on the signal enhancement in the aperture in VSAL.

Waveguide theory calculations were presented by Chen *et al.*[10] to explain the influence of aperture waveguide orientation on the power throughput of such waveguides.

It was shown, that the aperture with its longer side perpendicular to the laser diode active region has a higher power throughput due to a longer evanescence field decay length, while the aperture oriented along the active region has smaller power throughput. The interference of SPs with the incident photons has been also observed for this aperture. It is confirmed by the presence of two confined signals in the close vicinity of the aperture in the direction of electric field polarization. The participation of surface waves in the enhanced transmission of light through a subwavelength slit has been theoretically predicted,[11] and our observations are consistent with that model.

We do not consider the effect of surface plasmons excited on the tip on the near-field signal enhancement.[21,22] The calculated energy of surface plasmons on Pt nanoparticles (10-100nm diameter) is *ca* 4.5 eV,[21] which is much higher then the laser beam energy (1.9 eV), and in this case surface plasmons of the tip can not be excited.

In conclusion, localized surface plasmons on very small aperture lasers were observed using apertureless near-field microscopy. The interference of surface waves with transmitted through the aperture light accounts for the enhancement of the near-field signal in the aperture. We also have shown that the waveguides can be used to confine and enhance the light in VSALs. Different geometries of the apertures may result in the new near-field patterns, and stronger signals can be obtained when the SP excitation energy and the energy of incident light match.

BIBLIOGRAPHY

1. W.Hickel, B. Rothenhausler, and W. Knoll, J. Appl. Phys. **66**, 4832 (1989).

2. E. Krestchmann, Opt. Commun. **6**, 185 (1972).

3. L. Yin, V. K. Vlasko-Vlasov, A. Rydh, J. Pearson, U. Welp, S.-H. Chang, S. K. Gray, G. C. Schatz, D. B. Brown, and C. W. Kimball, Appl. Phys. Lett. **85**, 467 (2004).

4. H. F. Ghaemi, Tineke Thio, D. E. Grupp, T. W. Ebbesen, and H. J. Lezec, Phys. Rev. B **58**, 6779 (1998).

5. B. Hecht, H. Bielefeldt, L. Novotny, Y. Inouye, and D. W. Pohl, Phys. Rev. Lett. **77**, 1889 (1996).

6. S. Wang, S. Boussaad, and N. J. Tao, Rev. Sci. Inst. **72**, 3055 (2001).

7. M. Futamata, and S. Masuda, Anal. Science Suppl. **17**, i103 (2001).

8. I. Gontijo, M. Boroditsky, E. Yablonovitch, S. Keller, U. K. Mishra, and S. P. DenBaars, Phys. Rev. B **60**, 11564 (1999).

9. K. Okamoto, I. Niki, A. Shvartser, Y. Narukawa, T. Mukai, and A. Scherer, Nature Materials **3**, 601 (2004).

10. F. Chen, D. D. Stancil, and T. E. Schlesinger, J. Appl. Phys. **93**, 5871 (2003).

11. J. Lindberg, K. Lindfors, T. Setala, M. Kaivola, and A. T. Friberg, Optics Express **12**, 623 (2004).

12. A. Partovi, D. Peale, M. Wuttig, C. A.. Murray, George Zydzik, L. Hopkins, K. Baldwin, W. S. Hobson, J. Wynn, J. Lopata, L. Dhar, R. Chichester, and J. H.-J. Yeh, Appl. Phys. Lett. **75**, 1515 (1999).

13. F. Chen, A. Itagi, J. A. Bain, D. D. Stancil, T. E. Schlesinger, L. Stebounova, G. C. Walker, B. B. Akhremitchev, Appl. Phys. Lett. **83**, 3245 (2003).

14. F. Chen, J. Zhai, D. D. Stansil, and T. E. Schlesinger, Jpn. J. Appl. Phys. **40**, 1794 (2001).

15. B. B. Akhremitchev, Y. Sun, L. Stebounova, and G. C. Walker, Langmuir **18**, 5325 (2002).

16. Y. Murata, and S. Ohtani, J. Vac. Sci. Tech. **9**, 789 (1971).

17. D. R. Lide, *Handbook of Chemistry and Physics* (CRC Press, Inc. 1994).

18. J. R. Sambles, G. W. Bradbery, and F. Yang, *Contemporary Physics* **32**, 173 (1991).

19. H. Kano, S. Mizuguchi, and S. Kawata, J. Opt. Soc. Am. B **15**, 1381 (1998).

20. S. Kawata, *Near-Field Optics and Surface Plasmon Polaritons* (Springer-Verlag, Heidelberg, 2001).

21. P. Andre, F. Charra, M. P. Pileni, J. Appl. Phys. **91**, 3028 (2002).

22. E. Kryukov, Y.-K. Kim, and J. B. Ketterson, J. Appl. Phys. **82**, 5411 (1997).

5. IMAGING OF OPTICAL FIELD CONFINEMENT IN RIDGE WAVEGUIDES FABRICATED ON VERY-SMALL-APERTURE LASERS[§]

Optical field confinement in a ridge waveguide nanostructure ("C"-aperture) designed for ultrahigh-density recording was observed using an apertureless near-field scanning optical microscope. The aperture was fabricated on a commercial edge-emitting semiconductor laser as the light source. High-contrast near-field images at both 1× and 2× lock-in detection frequencies were obtained. The emission patterns are in agreement with theoretical simulation of such structures. A 90nm × 70nm full-width-half-maximum spot size was measured and is comparable to the ridge width of the aperture.

5.1. Introduction

Near-field optical recording could potentially increase current optical recording densities many-fold by breaking the diffraction limit.[1,2] In order to do so, a sub-wavelength metallic aperture could be used to produce optical spots much smaller than the wavelength of the light source. A metallic aperture can be microfabricated using a focused ion beam (FIB) etcher. The size of the aperture determines the spot size obtainable and therefore the recording density. Another proposed application of metallic apertures is in heat-assisted magnetic recording (HAMR) where

[§] This work has been published as Chen, F.; Itagi, A.; Bain, J. A.; Stancil, D. D.; Schlesinger, T. E.; Stebounova, L.; Walker, G. C.; Akhremitchev, B. B. Imaging of optical field confinement in ridge waveguides fabricated on very-small-aperture laser. *Appl. Phys. Lett.* **2003**, *83*, 3245-3247.

the magnetic medium is heated with a tiny optical spot to reduce the local coercivity.[3] To achieve a projected areal density of 1Tbit/in^2 in HAMR, the aperture has to be as small as 25 nm. However, the power throughput of these nanoapertures is a primary concern. As the aperture size decreases, the power delivered through the aperture also decreases rapidly. Conventional aperture designs often choose square apertures as the default geometry. In a previous study, we have shown the validity of treating the nanoapertures as cutoff waveguides.[4] This approach provides a first-order explanation for the exponential decay of the optical field inside the aperture and can be used to estimate the theoretical limit on the nanoaperture size useful for recording. In an unpublished calculation, it has been shown that conventional apertures have a fundamental limit suitable for reordering or as a heat source for <50 nm marks and hence motivate the requirement for more sophisticated aperture designs.[5]

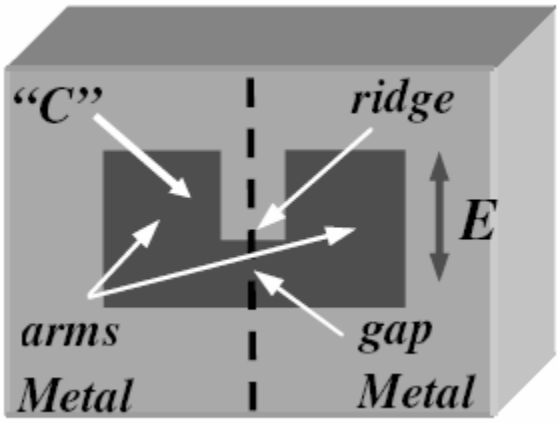

Figure 5-1 A ridge waveguide structure (C aperture) that can have high power throughput.

Recently some unconventional aperture structures such as the bowtie antenna structure[6] and "C"-shaped aperture[7] were suggested and actively studied due to their potential to achieve much higher throughput than conventional apertures. In their simulation work, Shi *et al.*[7] predicted a 1000× improvement in throughput for a C aperture with a 100 nm × 100 nm gap as compared to a simple 100 nm × 100 nm square aperture. These structures are intended to explore other mechanisms to increase the throughput. Rather than utilizing metallic walls only to guide the optical fields toward the exit, they have open structures combined with a narrow geometry to focus or confine the optical field. Figure 5-1 is a schematic diagram of a C aperture where the C shape is carved out of a metal layer with a finite thickness. This structure was described as a "ridge waveguide" [8] and we will refer to it as such in the following.

This structure has been simulated by Shi *et al.*[7] and Itagi *et al.*[9] using finite difference time domain (FDTD) methods. From these models, one concludes that the incident optical field is expected to form a confined spot under the narrow "ridge" in the "gap". At the same time the geometry of this structure includes large open areas, or "the arms" that are also exposed to the incident field $\boldsymbol{E}$. The advantage is that the overall dimension of the aperture is greater than the cutoff dimension for the fundamental mode of the waveguide. This therefore allows much higher throughput than a cutoff waveguide. The question is, how well will the optical field be confined under the ridge and therefore how one can achieve a small spot size. In this report, we will provide experimental evidence of the optical field confinement by studying the field distribution in the near-field of the ridge waveguide structure.

5.2. C aperture design and FDTD simulations

The structure being studied was fabricated on a very-small-aperture laser (VSAL). A VSAL is a near-field recording device that incorporates a nanoaperture directly onto a semiconductor laser.[10] Al was deposited onto the front facet of a commercial edge-emitting laser. The nanoaperture was fabricated using FIB to expose the active region beneath the coating.[11] The ridge waveguide structure fabricated is detailed in Figure 5-2.

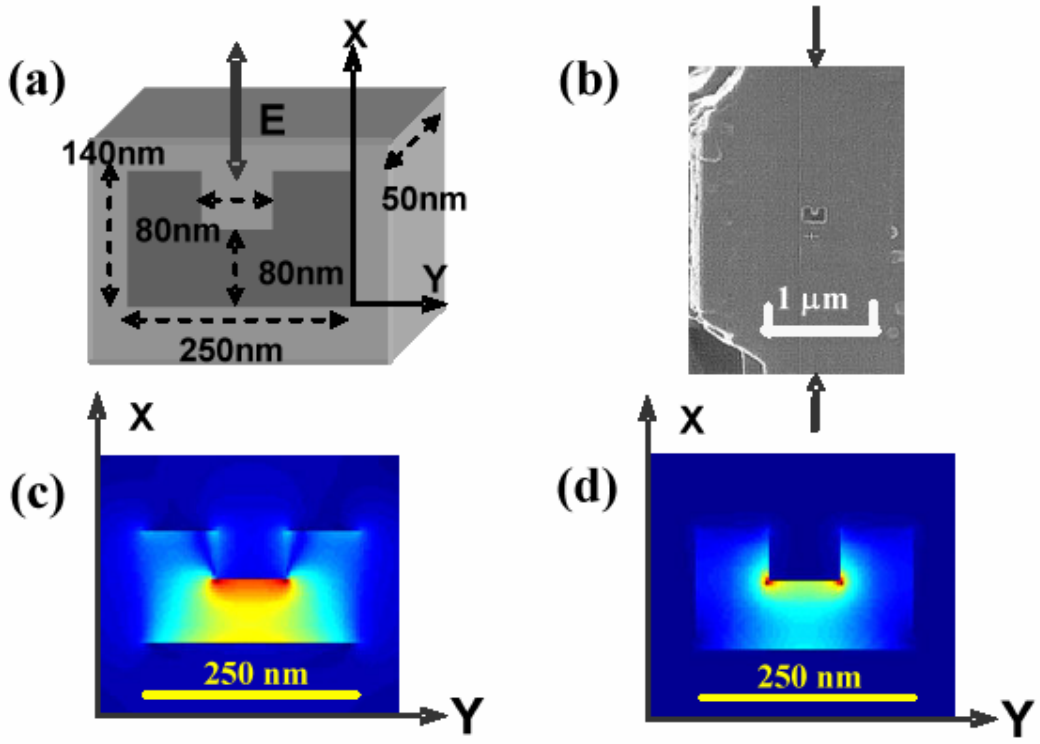

Figure 5-2 (a) Detailed geometry of a designed ridge waveguide structure, (b) FIB image of such a ridge waveguide fabricated on VSAL (arrow indicating active layer position); (c) and (d) are FDTD simulations of this ridge waveguide showing the E_x field structure (the dominant component) and total field E distribution at the exit plane of the aperture.

It has a gap area of 80 nm × 80 nm under the ridge, and the metal layer thickness is 50 nm. The *x*-polarized incident light propagates in the *z*-direction from the back to the front. Figure 5-2b is an FIB image of the VSAL with such an aperture fabricated over the active layer and where the arrows indicate the active layer position. The reason that the above geometry was chosen is that (1) an 80 nm × 80 nm gap is relatively easy to fabrication in the FIB, and (2) our FDTD simulation suggests that for an 80 nm × 80 nm gap area in a 50 nm thick Al at λ = 655 nm, a 250 nm × 140 nm outer dimension would have the highest throughput.

Both E_x and total E field intensity structures obtained with the FDTD simulation at the exit plane of the aperture are plotted in Figure 5-2c and Figure 5-2d, respectively. It is obvious that the majority of the predicted optical field is concentrated under the ridge while little is expected in the arms. The dominant field component in the gap is the E_x.

5.3. Optical near-field emission from very small C aperture laser

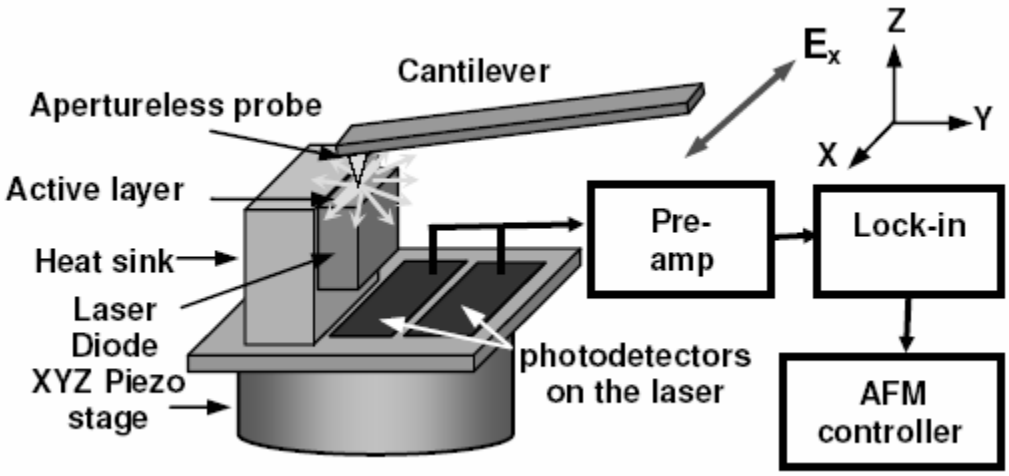

Figure 5-3 Detailed geometric relations of the apertureless NSOM components for ridge waveguide structure imaging. The structure is fabricated along the active layer.

The aperture fields are composed primarily of evanescent components that do not propagate. Therefore a near-field measurement has to be performed. It has been shown by Bachelot *et al.*[12] that apertureless near-field scanning optical microscopy (NSOM) can permit the near-field study of laser diodes in operation.By the same token, the optical field in the near-field of an aperture fabricated on a VSAL may be measured using an apertureless NSOM.Our apertureless NSOM was modified from a Digital Instruments (Santa Barbara, CA) multimode atomic force microscopy (AFM).[13] The basic principle of the measurement is illustrated in Figure 5-3.

The VSAL sample is mounted on an *XYZ* piezostage with the front facet of the laser perpendicular to the axis of the AFM tip. A Melles Griot (Carlsbad, CA) laser driver controls the laser emission in constant current mode and 655 nm light is emitted from the aperture. A platinum-coated silicon tip (MikroMasch, Tallinn, Estonia) is brought to proximity over the aperture and oscillated perpendicularly to the sample surface. The oscillation is near the resonant frequency of the cantilever f_r which is about 150 kHz. The near-field emission is then scattered by the very end of the probe that has a radius of curvature of about 50 nm. This converts some of the evanescent waves near the aperture to propagating waves scattered in all directions. The detectors used to detect the scattered light are the integrated photodetectors on the laser package. They are located near the back facet of the laser chip as indicated. The scattered light could reach the detector directly or *via* reflections from the surrounding surfaces such as the cantilever beam. The electrical signal from the detector is first preamplified and then lock-in detected at integer multiples of the tip oscillation frequency. Using the scanning function of the AFM, the tip-sample separation is controlled in intermittent contact mode. The near-field optical image is generated simultaneously with the surface topography image. The two images provide important complementary information.

Lock-in detection was carried out at both 1× and 2× the oscillation frequency (*1f* and *2f* detection) to obtain the near-field images. It has been suggested that *2f* detection is more sensitive to the scattered flux modulated only by the extremity of the probe, and therefore yields higher contrast and resolution.[14-16] Our results are summarized in Figure 5-4.

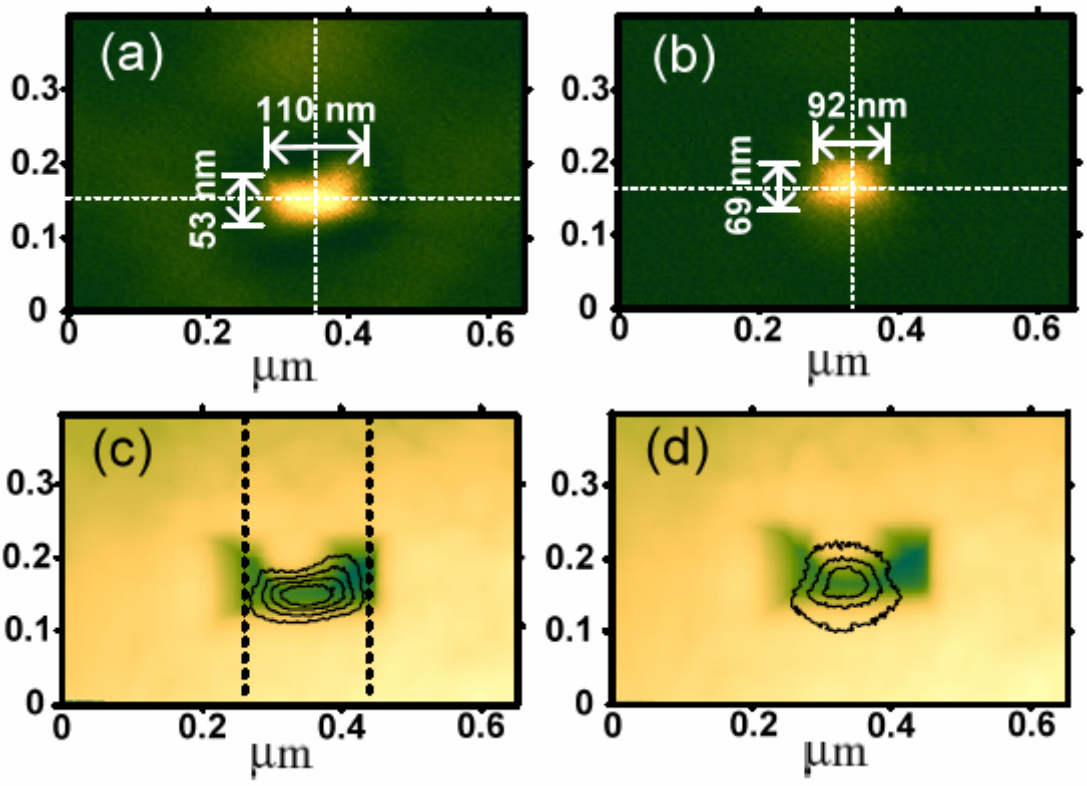

Figure 5-4 Observation of optical field confinement in the ridge waveguide: (a) Near-field image at *1f* detection; (b) near-field image at *2f* detection, (c) and (d) are the height images with optical intensity contours for *1f* and *2f*. Spot size confinement effect is clearly indicated.

Figure 5-4a-5-4d are the *1f* and *2f* detected near-field images, and their corresponding height images with optical intensity contours, respectively. From Figure 5-4a and 5-4b, clear optical field confinement can be observed in both *1f* and *2f* near-field emission patterns with the *2f* signal appearing more focused. Cross-section analysis was performed on the emission patterns along the crosshairs shown. The full width half maximum (FWHM) spot sizes in both x and y directions are indicated beside the near-field images. The data once again show that the optical spots are confined under the ridge. We expect that actual confinement of the electric field might be narrower than reported here. Measured distributions are usually widened by the finite size of the scatterer. It is also important to note that, in general, the tip may scatter different components to a lesser or greater extent. While we assume that our tip may be treated as a spherical scatterer, we note that the dominant field component is E_x for this structure and that, in any case, the model shows that both E and E_x are confined under the ridge. In Figure 5-4c, the dotted lines indicate the active layer width and its relative position in the structure. It should be pointed out that the active layer of the laser and, therefore, the incident beam is at least 0.2 μm wide in the horizontal direction. If the optical confinement did not exist, there would be observable signals filling the arms. We also superimposed the contours of light intensity for both *1f* and *2f* signals on top of the height image of the C aperture, shown in Figure 5-4c and Figure 5-4d. It can be observed that the spot width is roughly defined by the ridge width with some signals along the edges of the ridge. Little signal is observed in the arms. To check the repeatability of the above results, another ridge waveguide with slightly different dimensions was also fabricated and imaged. Similar optical confinement was again observed.

As an explanation for the confinement effect, we note that the near-field patterns in Figure 5-4 resemble the electric flux distribution between a charged probe tip and a conducting plane

brought near each other. In fact, an optical field propagating through a metallic waveguide would induce surface currents and surface charges. At the end of the narrow ridge, there would result a high charge density concentration due to the small radius of curvature. This induces large electric fields across the gap to the mirror charges on the edge. The charge polarities alternate and behave like oscillating dipoles. The direction of the induced field is predominantly along the direction of the incident field, therefore facilitating light throughput. Apparently, the smaller the ridge width and gap width, the better the field confinement.[9]

In conclusion, using apertureless NSOM, we have obtained high contrast near-field images of nanoaperture emissions. We observed strong evidence of optical field confinement by the ridge waveguide (C aperture) fabricated on a VSAL. 90nm FWHM spot size was obtained in the direction of the ridge width and 70nm in the other direction. This study is important because it reports the direct measurement of optical near-field emission from this type of nanoaperture structure and the results are consistent with theoretical predictions.

BIBLIOGRAPHY

1. E. Betzig and J. Trautman, Science **257**, 189 (1992).
2. E. Betzig, J. Trautman, and M. Kryder, Appl. Phys. Lett. **61**, 142 (1995).
3. T. McDaniel and W. Challener, Trans. Magn. Soc. Jpn. **2**, 316 (2002).
4. F. Chen, D. D. Stancil, and T. E. Schlesinger, J. Appl. Phys. **93**, 5871 (2003).
5. F. Chen, PhD Thesis, Carnegie Mellon University, 2003.
6. R. Grober, R. Schoelkopf, and D. Prober, Appl. Phys. Lett. **70**, 1354 (1997).
7. X. Shi, R. Thornton, and L. Hesselink, Proc. of SPIE **4342**, 320 (2001).
8. D. D. Stancil, A. Itagi, T. E. Schlesinger, J. Bain, and T. Rausch, US patent application No. 10/256809.
9. A. Itagi, D. Stancil, T. E. Schlesinger, and J. Bain, Appl. Phys. Lett. (to be published).
10. A. Partovi, D. Peale, M. Wuttig, C. Murray, G. Zydzik, L. Hopkins, K. Baldwin, W. Hobson, J. Wynn, J. Lopata, L. Dhar, R. Chichester, and J. Yeh, Appl. Phys. Lett. **75**, 1515 (1999).
11. F. Chen, J. Zhai, D. Stancil, and T. E. Schlesinger, Jpn. J. Appl. Phys. **40**, 1794 (2001).
12. R. Bachelot, G. Wurtz, and P. Royer, Appl. Phys. Lett. **73**, 3333 (1998).
13. B. B. Akhremichev, S. Pollack, and G. C. Walker, Langmuir **17**, 2774 (2001).
14. G. Wurtz, R. Bachelot, and P. Royer, Eur. Phys. J. AP. **5**, 269 (1999).
15. B. B. Akhremitchev, Y. Sun, L. Stebounova, and G. C. Walker, Langmuir **18**, 5325 (2002).
16. L. Stebounova, B. B. Akhremitchev, and G. C. Walker, Rev. Sci. Inst. **74**, 3670 (2003).

6. CONCLUDING REMARKS

Scanning near-field microscopy provides optical resolution far beyond the diffraction limit of conventional microscopy.[1] It has been used to characterize samples ranging from semiconductors to polymers to biological materials using electromagnetic radiation from ultraviolet to radio waves.[2-7] In this work, the development of chemically sensitive apertureless infrared near-field microscopy along with high-power output aperture-probe near-field microscopy is presented.

A new strategy to amplify weak scattered signal in apertureless infrared near-field microscopy was described and characterized in Chapter 2. Experimental results have proved that the near-field signal is amplified many fold using homodyne detection, and signal-to-noise ratio is greatly improved. The coupled dipoles model is described in Chapter 2. It has been used to explain the dependence of the near-field signal on the distance between the probe and the sample. The tip was represented as two scattering spheres, one sphere above another, and the results after applying this model indicate the electromagnetic field enhancement is 90 fold greater at the sharp apex of metallic probe tip.

Infrared near-field microscopy has been used to obtain submonolayer chemical sensitivity on a DNA sample (Chapter 3). Another way to reduce background contribution to the near-field signal and thus, improve signal-to-noise ratio, is described in Chapter 3. Due to the large spot size of the focused IR beam, a significant portion of the cantilever is illuminated, providing a background contribution to the detected scattered signal. It has been shown that the detection of the scattered signal at the twice the frequency of the probe's oscillation provides a convenient

way to extract the surface-specific signal. The near - field images collected at twice the frequency of the cantilever oscillation clearly demonstrate the chemical sensitivity of infrared near – field microscope. By collecting near-field images at different wavelengths in the phosphate absorption band it has been observed that the near-field signal follows the same wavelength dependence as the far-field absorption, further confirming that contrast in the near-field images is caused by varying chemical composition of a sample.

Another interesting study using apertureless near-field microscopy has been done on very small aperture lasers. These devices display an output 10^4 times that of tapered, metal-coated optical fiber probes, the most common light source for near-field scanning microscopy.[8] A higher-power light source may increase the signal-to-noise ratios and data rates of current applications as well as lead to the development of compact near-field microscopes. Chapter 4 demonstrates that surface plasmons can be used to enhance the emission of light from very small aperture lasers. New mechanisms of surface plasmons excitation applicable to such devices have been discussed. These mechanisms involve the energy transfer between semiconductor quantum wells and metal/dielectric surface plasmons. The preferred orientation of the rectangular aperture made on a laser diode covered with metal, with respect to the direction of electric field polarization, has been investigated in Chapter 4. It has been shown that the aperture with its longer side oriented perpendicular to the active layer of the laser diode has a higher power output in the near-field.

Chapter 5 continues the study of very small aperture lasers using apertureless near – field microscopy. Optical field confinement in a ridge waveguide nanostructure ("C"-aperture) designed for ultrahigh-density recording was observed using an apertureless near-field scanning optical microscope. A 1000× improvement in throughput for a C aperture with a 100 nm × 100 nm gap as compared to a simple 100 nm × 100 nm square aperture was predicted.[9] This structure

is intended to explore other mechanisms to increase the power throughput. 90 nm full width at half maximum spot size of the near – field signal was obtained in the direction of the ridge width and 70 nm in the other direction. This study is important because it reports the direct measurement of optical near-field emission from this type of nanoaperture structure and the results are consistent with theoretical predictions.

Future direction in the infrared near-field microscopy would be the study of fibrillar aggregates of proteins in the Amide I, Amide II, or Amide III wavelength region, in order to determine the structural and compositional properties of such aggregates. It would give an insight on the causes for the formation of the fibrils in human organs. Further development of the near - field microscopy to enable imaging in liquid would bring new possibilities for biological applications.

The near – field imaging of the optical emission patterns on very small aperture lasers with the aperture structure such as the "bowtie" antenna[10] would be the direct observation of the near – field signal enhancement by this aperture design.

Very small aperture lasers emitting at different wavelengths could be used as the near-field aperture probes with high output power.

BIBLIOGRAPHY

1. D. Courjon and C. Bainier, Rep. Prog. Phys. **57**, 989 (1994).

2. B. Hecht, B. Sick, U. P. Wild, V. Deckerd, R. Zenobi, O. J. F. Martin, and D. W. Pohl, J. Chem. Phys. **112**, 7761, (2000).

3. S. K. Buratto, Curr. Opin. Solid State Mater. Sci. **1**, 485 (1996).

4. R. C. Dunn, Chem. Rev. **99**, 2891 (1999).

5. P. F. Barbara, D. M. Adams, and D. B. O'Connor, Anu. Rev. Mater. Sci. **29**, 433 (1999).

6. J. D. McNeill, D. B. O'Connor, and P. F. Barbara, J. Chem. Phys. **112**, 7811 (2000).

7. N. F. van Nulst, J.-A. Veerman, M. F. Garcya-Parajo, and L. Kuipers, J. Chem Phys. **112**, 7799 (2000).

8. A. Partovi, D. Peale, M. Wuttig, C. A. Murray, G. Zydzik, L. Hopkins, K. Baldwin, W. S. Hobson, J. Wynn, J. Lopata, L. Dhar, R. Chichester, and J. H.-J. Yeh, Appl. Phys. Lett. **75,** 1515 (1999).

9. X. Shi, R. Thornton, and L. Hesselink, Proc. of SPIE **4342**, 320 (2001).

10. R. Grober, R. Schoelkopf, and D. Prober, Appl. Phys. Lett. **70**, 1354 (1997).